Journal of Hydrology 609 (2022) 127695

Contents lists available at ScienceDirect

Journal of Hydrology

journal homepage: www.elsevier.com/locate/jhydrol

Research papers

Interaction of basin-scale topography- and salinity-driven groundwater flow in synthetic and real hydrogeological systems

Attila Galsa [a,*], Ádám Tóth [b], Márk Szijártó [a], Daniele Pedretti [c], Judit Mádl-Szőnyi [b]

[a] Department of Geophysics and Space Science, Institute of Geography and Earth Sciences, ELTE Eötvös Loránd University, Budapest, Hungary
[b] József and Erzsébet Tóth Endowed Hydrogeology Chair, Department of Geology, Institute of Geography and Earth Sciences, ELTE Eötvös Loránd University, Budapest, Hungary
[c] Dipartimento di Scienze della Terra "A. Desio", Università degli Studi di Milano, Milan, Italy

ARTICLE INFO

This manuscript was handled by C. Corradini, Editor-in-Chief

Keywords:
Mixed topohaline convection
Salinity-driven groundwater flow
Topography-driven groundwater flow
Numerical modelling

ABSTRACT

Salinization of groundwater has endangered e.g. drinking water supply, agricultural cultivation, groundwater-dependent ecosystems, geothermal energy supply, thermal and hydrocarbon well production to a rising degree. In order to investigate the problem of coupled topography- and salinity-driven groundwater flow on a basin-scale, a systematic simulation set has been carried out in a synthetic numerical model. Detailed sensitivity analysis was completed to reveal the effect of the salinity, permeability, permeability heterogeneity and anisotropy, mechanical dispersivity and water table head on the salt concentration field and the flow pattern. It was established that a saline dome with slow inner convection formed beneath the discharge zone in the base model due to the topography-driven regional fresh groundwater flow. An increase in the salinity or the anisotropy or decrease in the water table variation weakens the role of the forced convection driven by the topography, thus facilitating the formation of a saline, dense, sluggish layer in the deepest zone of the basin. In the studied parameter range, the variation in permeability and dispersivity affects the shape of the saltwater dome to less degree. However, the decrease in permeability and/or the increase in dispersivity advantage the homogenization of the salt concentration within the saline zone and strengthen the coupling between the saltwater and freshwater zone by growing the relative role of diffusion and transverse dispersion, respectively. The interaction of the topography-driven forced and salinity driven free convection was investigated along a real hydrological section in Hungary. Simulation elucidated the fresh, brackish and saline character of the water sampled the different hydrostratigraphic units by revealing the connection between the topography-driven upper siliciclastic aquifer and the lower confined karstic aquifer through faults in high-salinity clayey aquitard. The current study improves the understanding of the interaction between the topography-driven forced and the salinity-driven free convection, i.e. topohaline convection, especially in basin-scale groundwater flow systems.

1. Introduction

Hydrogeological problems that we have to solve in practical tasks often refer to complex systems, but our solutions are necessarily simplified. Unfortunately, it means that we neglect many effects and processes and, on the contrary, put in the focus what we think is significant. To exclude these uncertainties and better understand some physical fluid flow processes and their interactions, we started a systematic analysis of superimposed fluid driving forces and their impacts on basin-scale flow patterns. We have already examined the combination of topography and thermal buoyancy that drive groundwater flow in a theoretical basin to better understand the influencing factors and the consequences of the interaction (Szijártó et al., 2019). The lesson learnt from this systematic theoretical analysis, we applied to a real hydrogeological system focusing on these driving forces (Szijártó et al., 2021). In this paper, we continue the analysis with the interactions of topography and salinity as driving forces of fluids on basin-scale flow systems and demonstrate it for an actual hydrogeological situation without trying to extend the problem to any other driving force.

The importance and understanding of salt transport processes in groundwater flow systems has developed parallel to the increasing natural resource demands of humankind. In coastal environments, the rising number and yield of wells producing freshwater entail the subsurface transgression of sea water and subsequent deterioration of water

* Corresponding author.
E-mail address: attila.galsa@ttk.elte.hu (A. Galsa).

https://doi.org/10.1016/j.jhydrol.2022.127695
Received 12 May 2021; Received in revised form 16 February 2022; Accepted 4 March 2022
Available online 9 March 2022

quality has become a daily problem of inhabitants living near the coastlines (e.g. Barlow and Reichard, 2010; Werner et al., 2013; Hussain et al., 2019). In an inland environment, salinization triggered by groundwater overexploitation and pumping deeper and more saline reserves gives difficulties for agriculture, drinking water supply and the groundwater-dependent ecosystem protection (e.g. Jalali, 2007; Rodríguez-Rodríguez and Benavente, 2008; Herbert et al., 2015; McFarlane et al., 2017; Payen et al., 2016; Schuler et al., 2018; Singh, 2020). Interaction of salt and fresh groundwater can lead to carbonate dissolution resulting in permeability increase and extended reservoirs for hydrocarbon and thermal water production (Dublyansky, 1995; Kambesis and Coke, 2013; He et al., 2017; Zhang et al., 2020a; Smith et al., 2021). On the other hand, it can trigger sinkhole development causing serious environmental problems and damage (Oz et al., 2016; Karaki et al., 2019). The long-term negative impact of salinization on aquifers may be exacerbated by the effects of climate change (Havril et al., 2018), e.g. in terms of sea level rising or change in intensity–duration–frequency of precipitation events (e.g. De Paola et al., 2014; Sun et al., 2019). In addition, lithium recovery from brine attempts to satisfy the increasing requirements of the battery industry (e.g. Kesler et al., 2012; Marazuela et al., 2018; García-Gil et al., 2019).

Dissolved solids content increases the water density; hence it affects the groundwater flow driven by buoyancy force. Nield (1968) analytically determined the conditions of the onset of haline convection in a homogeneous, horizontal infinite porous layer, and Van Dam et al. (2009) uncovered the first field documentation of precipitation-induced saltwater fingering as a manifestation of natural free convection in a porous medium. However, the water table elevation varies from place to place, thus the topography-driven groundwater flow is always present in the upper part of the terrestrial basins (Tóth, 2009). Therefore, it also acts in these terrestrial environments with elevated dissolved solid content. Consequently, these cases require mathematical models (typically, numerical models) to evaluate the coupled effects of topography- and salinity-driven groundwater flow.

The concept of coupled topography- and salinity-driven groundwater flow has been adopted to explain the high salt content of the submarine groundwater discharge (SGD) on a local scale (Konikow et al., 2013), and to elucidate the variability and the distance of SGD in a heterogeneous coastal volcanic aquifer near the Big Island of Hawaii, USA (Kreyns et al., 2020). Duffy and Al-Hassan (1988) revealed the groundwater circulation in a homogeneous medium as a balance between the rainwater recharge in surrounding mountains and the saltwater counter flow beneath the playa in the Great Basin, Utah, USA. The two-dimensional, homogeneous and isotropic numerical model was recalculated using multicomponent reactive transport simulations to infer the evolution of the evaporite precipitation and brine composition (Hamann et al., 2015). Topography-driven forced and salinity-driven free convection processes were modelled in a simple geological environment to trace the brine infiltration beneath a saline disposal basin in Australia (Simmons and Narayan, 1997). Zhang et al. (2020b) presented a sensitivity analysis to study the effect of the salinity, the hydraulic conductivity and the dispersivity on the positions of stagnation points and the hierarchy of the groundwater flow system. However, it seems from the published papers that topography effects are examined on a local scale or for simple basins, but they are commonly neglected. Therefore, some of the models remained oversimplified in terms of omittance of variations in topography and water table.

Although numerical models are acknowledged tools to quantify the interaction of topography- and salinity-driven groundwater flow, several questions are still unresolved regarding the sensitivity of these models to the key parameters feeding the governing equations. Small variations in critical parameters, such as relative density differences due to salinity, variations of intrinsic permeability, anisotropy and mechanical dispersivity or change in water table amplitude may generate great deviations in model outputs. As such, given the ubiquitously difficult aquifer characterization that renders model parameterization always uncertain, high sensitivity to model parameters can create high uncertainty in the decisions to be made about the water management of an aquifer. While disentangling the model response to the input parameters is therefore of the uppermost importance, this task is in turn severely complicated by the computational burden required to resolve the nonlinear fully coupled density-dependent groundwater flow equations.

The main aim of this paper is to investigate, through detailed numerical modelling, how the interaction of topography-driven forced and salinity-driven free convection and the different model parameters influence the salt concentration and groundwater flow pattern at basin-scales and thus how the decisions made from the model responses may vary depending on the model sensitivity. Other fluid driving forces, e.g. temperature difference, compaction, compression, were neglected in order to focus on and highlight the interaction of topography- and salinity-driven regional groundwater flow and systematically examine the effects of this interaction firstly. Once the processes and phenomena are comprehensively understood and synthesized, other fluid driving processes can also be coupled. Therefore, in the first part of the paper, a two-dimensional, synthetic simulation set is presented, where the effect of salinity (dissolved solid content), permeability, depth-dependence and anisotropy of permeability, dispersivity and water table amplitude is qualified and quantified systematically by monitoring parameters, e.g. the Darcy flux and the salt concentration for both the entire basin and the fresh/saltwater zones. In the second part, the mixed topohaline convection simulation is carried out to demonstrate its effect in a real environment, along a hydrogeological section in Hungary based on Mádl-Szőnyi et al. (2019). The fundamental goal is to reveal the evolution of marine-origin pore water and to explain the formation of the fresh-, brackish and saltwater saturated units on a basin scale.

2. Materials and methods

2.1. Model development

The solution of the combined topography- and salinity-driven groundwater flow requires the coupled handling of the continuity equation (1), the Darcy's Law (2) and the mass transport equation (3) governing the mass conservation, the momentum conservation and the transport of the dissolved solid matter by advection, molecular diffusion and mechanical dispersion, respectively (Delgado, 2012; Nield and Bejan, 2017),

$$\Phi \frac{\partial \rho_w}{\partial t} + \nabla(\rho_w \boldsymbol{q}) = 0 \tag{1}$$

$$\boldsymbol{q} = -\frac{\boldsymbol{k}}{\mu}[\nabla p - \rho_w \boldsymbol{g}] \tag{2}$$

$$\Phi \frac{\partial c}{\partial t} = -\boldsymbol{q}\nabla c + \nabla\left[\left(D_{diff}\boldsymbol{I} + \boldsymbol{D_{disp}}\right)\nabla c\right] \tag{3}$$

where $\mathbf{q}$, p and c denote the unknown Darcy flux, the pressure and the dissolved salt concentration, while Φ, $\mathbf{k}$, μ, $\mathbf{g}$, D_{diff}, $\mathbf{D_{disp}}$, t and $\mathbf{I}$ are the porosity, the diagonal permeability tensor, the dynamic viscosity of the water, the gravitational acceleration, the molecular diffusion, the mechanical dispersion, the time and the identity matrix, respectively. The parameters of the base model are summarized in Table 1. The salinity-dependence of the viscosity was neglected in the course of the simulation, the dispersion tensor was defined by the longitudinal and the transverse dispersivity, α_L and α_T, respectively. The transverse dispersivity was affixed to the longitudinal one, $\alpha_T = \alpha_L/10$. The salt content was characterized by the non-dimensional concentration ranging between $c = 0$ and 1 to focus on the density variation of the water. A simple linear relation was supposed between the water density and the concentration (e.g. Duffy and Al-Hassan 1988, Nield and Bejan 2017),

Table 1
Parameters of the base model.

Description	Symbol	Value	Unit
Porosity	Φ	0.1	1
Reference water density	ρ_0	1000	kg/m^3
Dynamic viscosity of the water	μ	10^{-3}	Pa s
Molecular diffusion	D_{diff}	10^{-9}	m^2/s
Relative density difference	β	0.01	1
Horizontal permeability of the matrix	k_x	10^{-12}	m^2
Factor of depth-dependent permeability	γ	1	1
Permeability anisotropy coefficient	ε	1	1
Longitudinal dispersivity	α_L	0	m
Transverse dispersivity	α_T	0	m
Water level amplitude	A	50	m

$$\rho_w = \rho_0(1+\beta c) \tag{4}$$

where $\rho_0 = 1000$ kg/m^3 is the freshwater density and β denotes the relative density difference between freshwater ($c = 0$) and saltwater ($c = 1$).

A simple two-dimensional numerical model was built to reveal the physical background of salinity transport. The basin-scale model is characterized with a length of $L = 40$ km and a mean depth of $d = 5$ km (Fig. 1) to test the outcomes of synthetic simulations for a real hydrogeological system. The boundary conditions for the flow were no-flow along the sidewalls and the bottom, while the regional groundwater flow was driven by a cosinusoid water table (e.g. Domenico and Palciauskas, 1973; Wang et al., 2015; Zhang et al., 2018),

$$z_{wt}(x) = -A\cdot cos\left(\frac{\pi x}{L}\right) \tag{5}$$

with an amplitude of $A = 50$ m, where x denotes the horizontal coordinate. The water table, z_{wt} corresponds to the top of the model domain. No-flux boundary conditions for the concentration were prescribed along the sidewalls, while the concentration was fixed along the horizontal boundaries. It was $c = 1$ at the bottom and $c = 0$ on the surface, thus diffusive and dispersive flux was allowed across the horizontal boundaries. The former represents salinity influx from a deep impervious formation, and the latter symbolizes e.g. the freshwater infiltration and the salt precipitation from the groundwater. The initial condition for the flow was obtained from Eqs. (1)–(2) with reference water density (Fig. 1.a), and the initial condition for the concentration was calculated from Eq. (3) without the advection term ($\mathbf{q} = 0$), which is the solution of the diffuse problem resulting in linear vertical concentration profile (Fig. 1.b).

The coupled problem (Eq. (1)–(3)) was solved by COMSOL Multiphysics v4.2, a finite element numerical software package (Zimmermann, 2006. The model domain was discretized by triangle elements with a maximum size of 100 m and 8 boundary layer elements were used to minimize the inaccuracy due to the weak resolution of the high gradient zones. Thus, the mesh consisted of 57,159 finite elements for the base model, which varied between 56,880–80,023 as the water table amplitude was changed from 0 m to 500 m. The pressure and the concentration were discretized within the elements by quadratic and linear polynomials, respectively. Simulations were run until models reached the stationary solution, which required typically 1 Myr, ranging from 0.5 to 50 Myr (e.g. for low permeability, high permeability anisotropy or slight water table amplitude). Initial time steps were increased exponentially to 1000 yr to stabilize the transition effects, after that the maximum time step was fixed as 100 yr. Simulations were run on an Intel Workstation with 24 cores, requiring approx. 1–2 days CPU time and 4 GB memory for one model. Before the synthetic simulation set, the coupled model was expansively tested and confirmed in a horizontal and inclined layer, and solutions were compared with the analytical and numerical results of Weatherill et al. (2004). Tests resulted in perfect accordance focusing on the onset (critical Rayleigh number) and the form (transition from multi- to unicellular convection) of free haline convection.

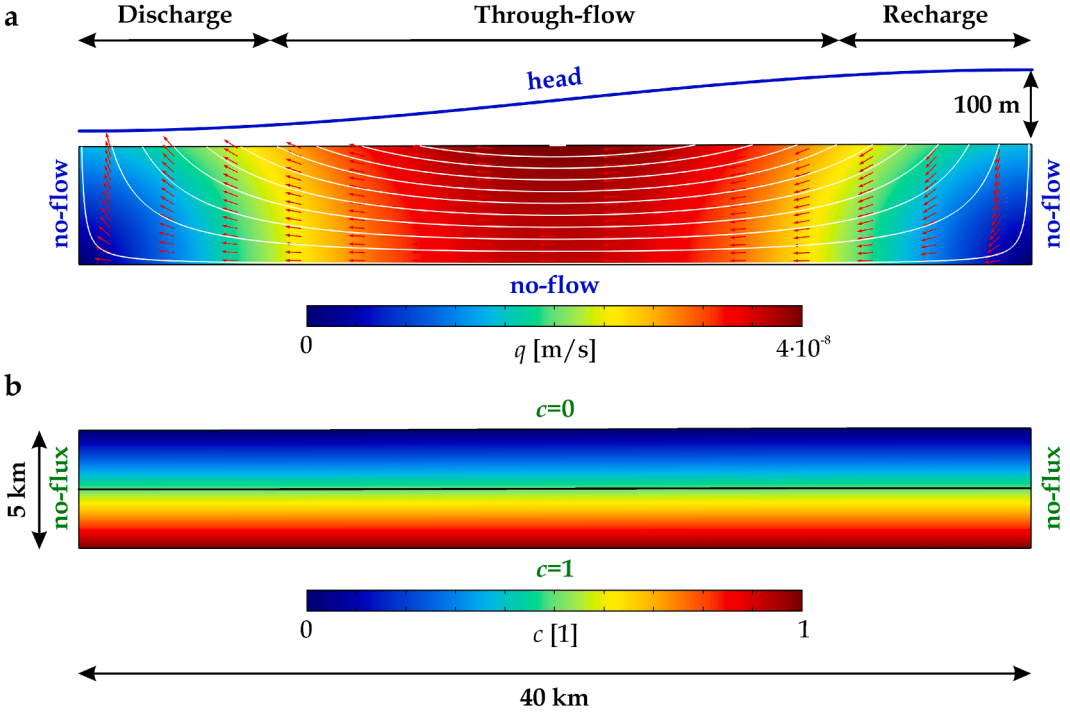

Fig. 1. Boundary and initial conditions for (a) the flow (blue) and (b) the salt concentration (green) in the base model (Table 1). (a) Streamlines of the Darcy flux (white) are magnitude controlled, red arrows illustrate the flow direction. (b) Isocontour of $c = 0.5$ (black line) represents the boundary between the saltwater and the freshwater zone. The model length is 40 km, the average model depth is 5 km, the vertical exaggeration is 1.

2.2. Model parameterization

Firstly, we systematically investigated the effect of the following relevant parameters (Table 2) resulting in 56 time-dependent models:.

1. the relative density difference due to salinity, β;
2. the permeability, *k*;
3. the factor of depth-dependence of permeability, γ;
4. the permeability anisotropy, ε;
5. the mechanical dispersivity, α_L and α_T; and
6. the water level amplitude, *A*.

The six selected parameters are usually uncertain given the limited characterization and exhibit strong scale dependency. For instance, the salinity of groundwaters may vary both in time and space. In Hungary, it is typical that the salt concentration increases with depth owing to the deep, marine sedimentary environment, while salinity is lower in shallow strata complexes due to lacustrine sedimentation and the intense meteoric water infiltration (e.g. Varsányi and Ó.Kovács, 2009; Szocs et al., 2013). In general, the groundwater salinity can vary from 0 to even 40% including fresh, brackish, saline and brine waters (Deming, 2002). In this paper, the effect of salinity on the water density is parameterized by a factor of β, which presents the relative density increase of the water. The aquifer permeability (or hydraulic conductivity) can vary over several orders of magnitude in relatively short spatial scales to the effects of geological heterogeneity (Sanchez-Vila et al., 2006; Pedretti et al., 2016; Liu et al., 2016). One of the most common heterogeneities of permeability is its pressure-dependence (Ehrenberg and Nadeau, 2005). Permeability decreasing exponentially with depth was defined by

$$k(z) = k_0 exp\left(ln\gamma \cdot \frac{z}{d}\right) \quad (6)$$

to characterize the pressure-dependence of the permeability (Jiang et al. 2009; Jiang et al., 2011), where k_0 denotes the surface permeability and z is the vertical coordinate pointing upwards. Anisotropy also controls the time evolution of flow and transport patterns in aquifers and depends on the nature and connectivity of the hydrogeological bodies (Cirpka et al., 2015; Pedretti et al., 2014). In siliciclastic sedimentary basins, where the sub-horizontal aquifer and aquitard layers alternate, the effective hydraulic conductivity strongly depends on the flow direction. The horizontal permeability, in such environments, can exceed the vertical permeability by several orders of magnitude (e.g. Galsa, 1997; Hoque and Burgess, 2020). Mechanical dispersion is present in the subsurface both in microscopic scale (grain size) and local scale (e.g. quasi-impermeable zones, lens). In aquifers (e.g. fractured media, siliciclastic and fluvial sediments), the longitudinal dispersivity is scale-dependent (Gao et al., 2012) and varies within a wide range (Gelhar et al., 1992; Schulze-Makuch, 2005; Vanderborght and Vereecken, 2007). The variation of the water level influences both the flow pattern and the salinity of the groundwater as one of the main driving forces (e.g. Tóth, 2009).

The influence of forming dense, saline zone/layer on the concentration field and the flow pattern was studied both qualitatively and quantitatively. Monitoring parameters were defined to characterize the groundwater flow system by the average Darcy flux (q_{av}), concentration (c_{av}), hydraulic head (h_{av}), as well as the relative area (A_s, A_f), the Darcy flux (q_s, q_f) and the concentration (c_s, c_f) computed for both the saltwater (subscript *s*) and the freshwater (subscript *f*) zone. The salt- and freshwater zones were separated by an arbitrary boundary of the solute content of $c = 0.5$. After the synthetic numerical simulations, the topography- and salinity-driven groundwater flow model was applied along a 2D hydrogeological section in Hungary taking into consideration the outcome of the synthetic model runs.

Table 2
Studied parameters.

Description	Symbol	Value	Unit
Relative density difference	β	0–0.2	1
Matrix permeability	*k*	10^{-14}–10^{-12}	m^2
Factor of depth-dependent permeability	γ	1–100	1
Permeability anisotropy coefficient	ε	1–1000	1
Longitudinal dispersivity	α_L (=10α_T)	0–100	m
Water level amplitude	*A*	0–500	m

3. Synthetic model results

3.1. Effect of relative density difference

As a first step, the effect of density increase due to salinity on the concentration field and the flow pattern was studied. The results show that the saltwater is swept out from the basin by the topography-driven groundwater flow, when $\beta = 0$, i.e. the water density is independent of the salt content (Fig. 2.a). A shrank zone beneath the discharge area can survive the regional freshwater circulation near the stagnation point (see e.g. An et al., 2015). Even though the saltwater is denser by only 1%, an extended saline zone ($c \geq 0.5$, contoured by a black line) forms beneath the discharge area in the base model (Fig. 2.b, Table 1). The concentration distribution within the saline zone is rather diffuse suggesting that there is no intense inner flow. As the salt content (i.e. water density due to salinity) increases, a dense layer evolves right above the model bottom (Fig. 2.d–g), which consequently reduces the diffuse transport from the base below resulting in an average concentration decrease in the basin.

Fig. 3 illustrates how the dense, saline zone modifies the regional, unidirectional flow pattern. When the concentration-dependence of the water density is neglected (Fig. 3.a), the Darcy flux field is equivalent to the solution of the simple Darcy flow (see Fig. 1.a). When the water density is not neglected (Fig. 3.b–d), the flow field strongly depends on the presence of the saline zone. The most striking influence of the saline zone on the flow pattern is that the topography-driven regional flow is suppressed, but the magnitude of the Darcy flux is not affected by the saline dome. On the other hand, slow circulation forms within the saltwater domain. This sluggish inner convection has opposite vorticity compared to the regional groundwater flow. The pattern of the inner convection depends strongly on the saline content, as measured by β. The higher the salinity contrast with the freshwater, the more pronounced the recirculation zone. Note that $\beta = 3\%$ produces an inner convection zone about two times more extended compared to $\beta = 1\%$. The model is therefore highly sensitive to limited salinity changes.

The given problem of topography- and salinity-driven groundwater flow tends towards a stationary solution, which is plotted against the relative density difference, β (Fig. 4). As the water density increases (see Eq. (4)) from $\beta = 0$ to 0.2, the domain-averaged Darcy flux (q_{av}) is reduced by 43% (Fig. 4.a). The domain-averaged concentration (c_{av}) shows a non-monotonic character with a maximum at about $\beta = 2$–3% (Fig. 4.b), when a considerable saltwater zone forms beneath the discharge area (Fig. 2.c). At a lower value of β, the salt content cannot resist the topography-driven groundwater flow, while at a higher value of β a thin, dense salty layer evolves in the deepest part of the basin. The domain-averaged hydraulic head (h_{av}) becomes more negative owing to the increasing water density (Fig. 4.c).

The specific behaviour of the saltwater and freshwater zone separated by the arbitrary isocontour of $c = 0.5$ was also investigated. As β increases, the relative area of the dense, saline zone (A_s, the area normed by the total area of the basin) shrinks, apart from the model of $\beta = 0$, when the saltwater is swept out from the basin (Fig. 2.a and 4.d). On the contrary, the relative area of the complementary freshwater zone, A_f (also normed by the total area of the basin) increases in the same way as A_s decreases. Fig. 4.e illustrates that the inner convective velocity of the saltwater zone (q_s) is lower up to about two orders of magnitude

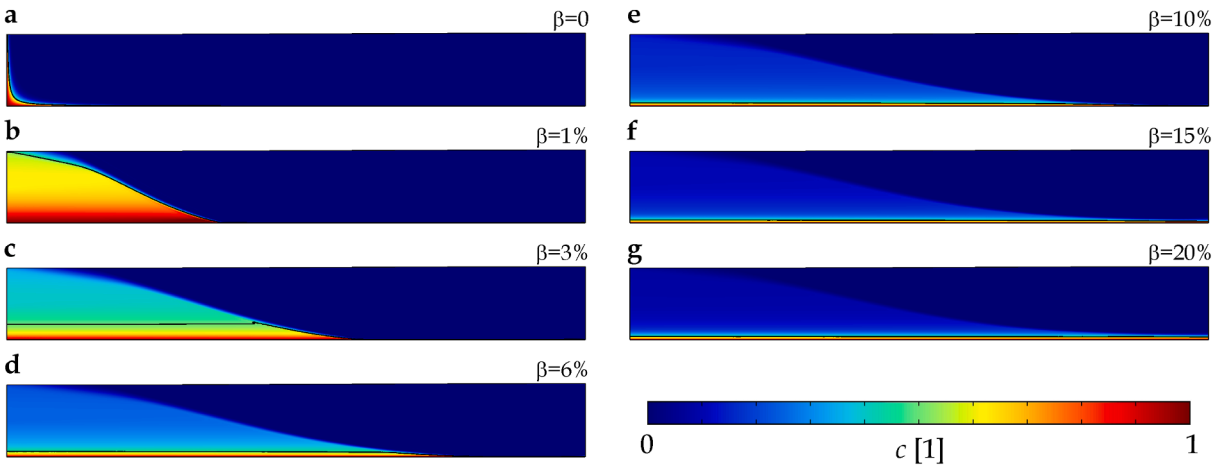

Fig. 2. Stationary solution of salt concentration at different relative density differences, β = 0–20%. Other parameters are defined in the base model (Table 1). Black isocontour of $c = 0.5$ represents the boundary of the saltwater and the freshwater zones.

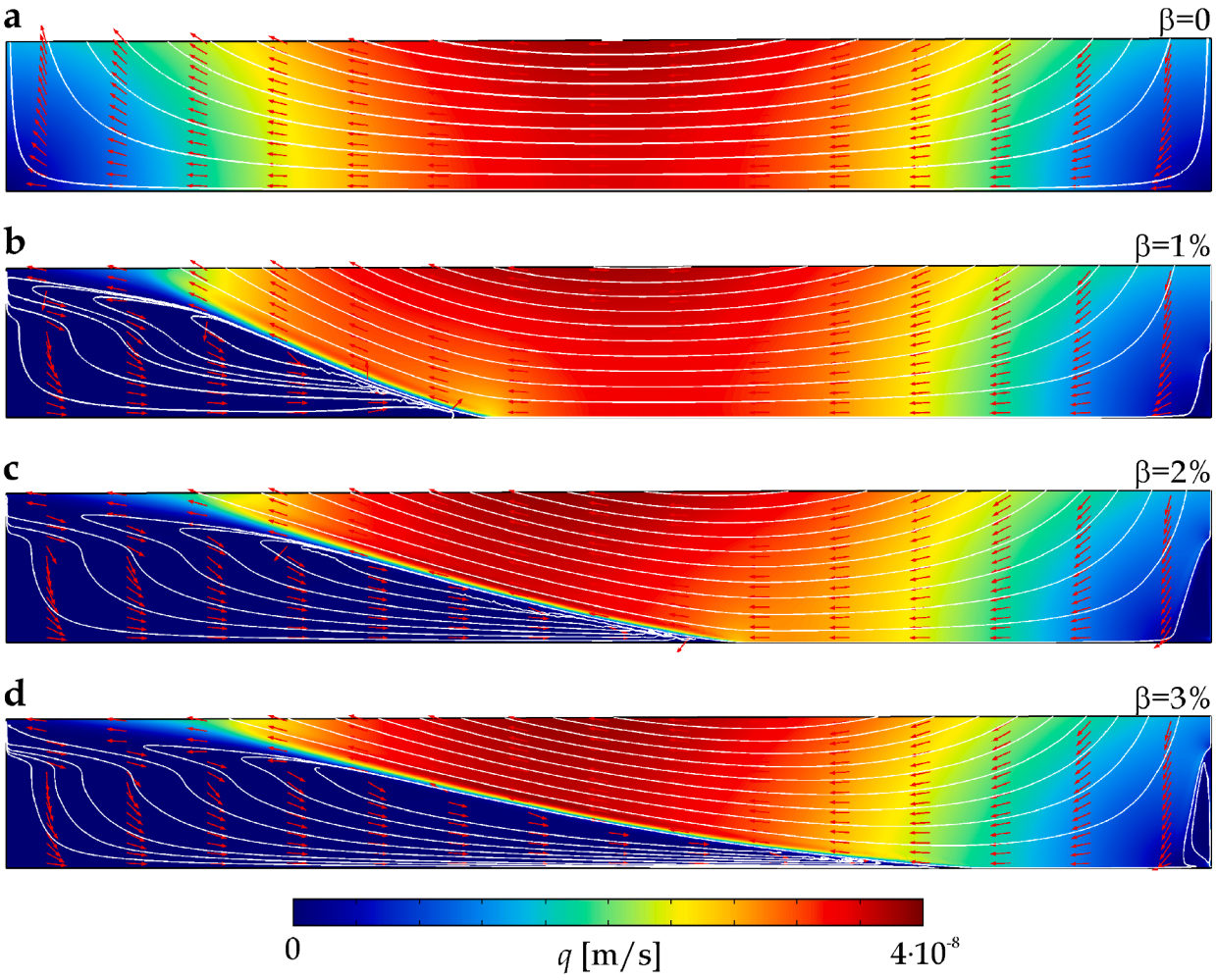

Fig. 3. Darcy flux for different relative density differences due to salinity at $t = 100$ kyr. Streamlines (white – not magnitude controlled) and arrows (red – normalized) represent the flow direction.

compared to the velocity of the freshwater zone (q_f), which remains quite constant ($q_f \approx 2 \cdot 10^{-8}$ m/s). Specifically, the minimum saltwater velocity of $q_s = 3 \cdot 10^{-10}$ m/s was found when β = 2%, i.e. at the peak of maximum domain-averaged concentration, c_{av}. This point also corresponds to the lowest average concentration of the dense zone ($c_s \approx 0.65$) (Fig. 4.f), when an extended saltwater dome with thick transition zone forms beneath the discharge zone (Fig. 2.c).

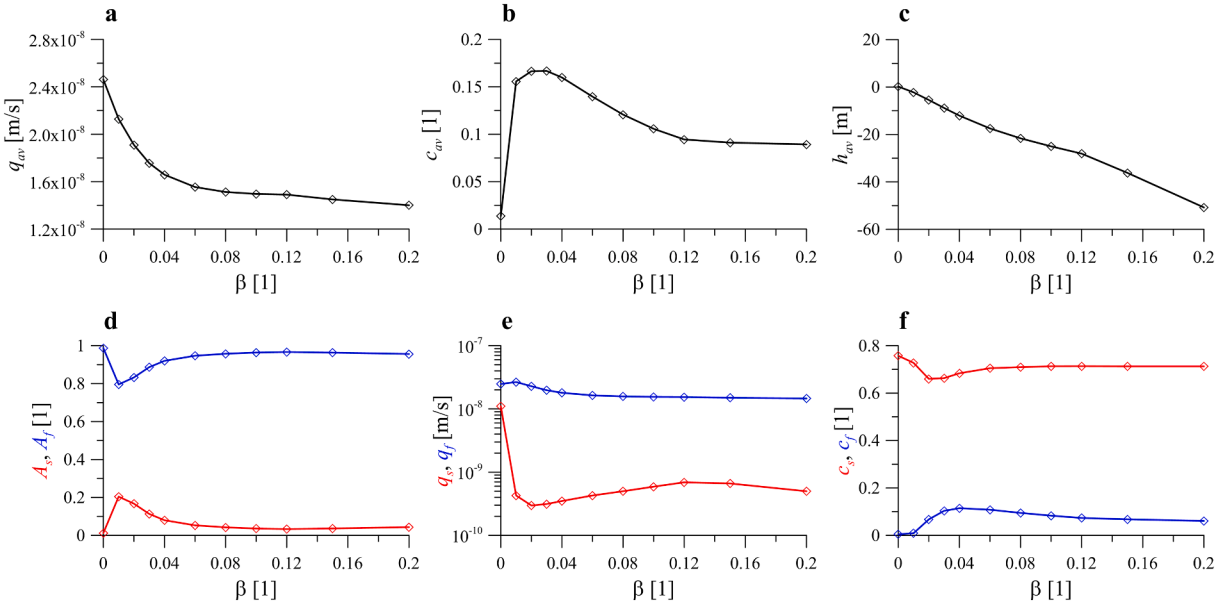

Fig. 4. Stationary solutions of the monitoring parameters plotted against the relative density contrast, β. (a) The average Darcy flux, (b) the average salt concentration and (c) the average hydraulic head. (d) The relative area, (e) the Darcy flux and (f) the concentration averaged for the saltwater (red) and the freshwater (blue) zones.

3.2. Effect of permeability

3.2.1. Permeability in a homogeneous and isotropic medium

The role of rock permeability on the salinity was investigated using the base model (Table 1), while the permeability (horizontal and vertical) was decreased from $k = 10^{-12}$ m^2 to 10^{-14} m^2. Fig. 5 illustrates that the change in permeability has no drastic influence on the salt concentration field. By decreasing the permeability, the flow linearly slows down (Fig. 6.a), according to Eq. (2). When the Darcy flux is reduced in the freshwater zone, the diffusion flux across the boundary of the salt- and freshwater zones is retained. Lower diffusion flux from the saltwater zone results in higher salt content (Fig. 6.b) and a more homogeneous concentration field (Fig. 5.a–d). As the average salt content increases, the hydraulic head decreases due to the enhanced water density (Fig. 6.c).

Decreasing the permeability from $k = 10^{-13}$ m^2 to 10^{-14} m^2, the diffusion flux becomes commensurable to the order of advection, thus the diffusion zone between the salt- and freshwater thickens (Fig. 5.d–g). A thickening diffusion zone appears above the model bottom, as well. While the change in permeability by two orders of magnitude drives an equal reduction in the average Darcy flux, the maximum of the diffusion flux reduces by only a factor of 5, specifically from $8{\cdot}10^{-11}$ to $1.4{\cdot}10^{-11}$ m/s.

The permeability reduction influences the Darcy flux of the saltwater and freshwater zones in a different manner (Fig. 6.e). The flow slows down in both zones, but the gradient of the Darcy flux curve is higher for the freshwater zone than the saltwater zone (i.e. $dq_f/dk > dq_s/dk$), consequently, the difference in the Darcy flux decreases to one order of magnitude. The effect of two processes appears both in the concentration and the relative area curves (Fig. 6.d and f). The homogenization (in the cases of $k = 10^{-12}$–10^{-13} m^2) increases the salt content and the area of the saline zone. Then the diffusion zone thickening (in the cases of $k = 10^{-13}$–10^{-14} m^2) hinders the rate of the area growth, and it leads to a slight concentration decrease within the saltwater zone. Nevertheless, the average salt content of the basin shows a slight increase (Fig. 6.b) owing to the slowing down regional groundwater flow.

3.2.2. Permeability heterogeneity

Owing to the increasing pressure, the permeability shows a decrease downwards both in carbonates and sandstones, which is frequently

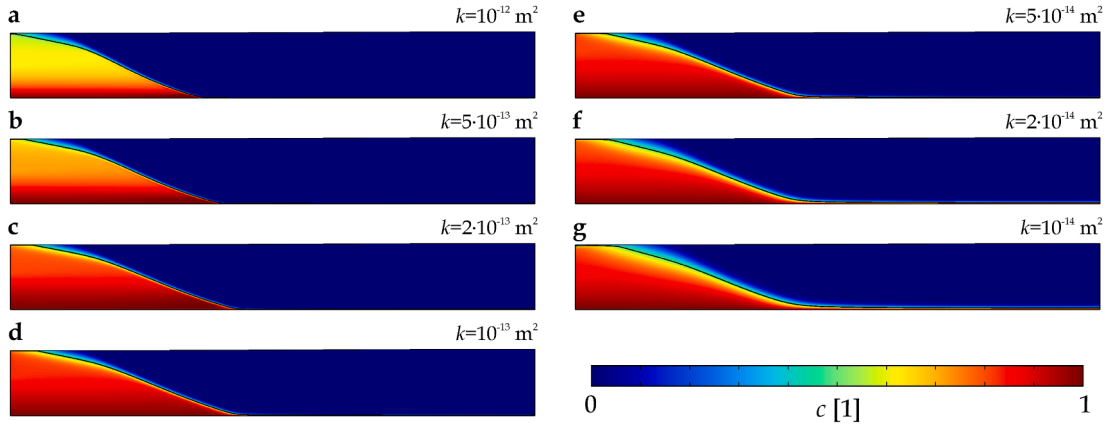

Fig. 5. Stationary solution of salt concentration at different permeability of the matrix, $k = 10^{-12}$–10^{-14} m^2. Other parameters are defined in the base model (Table 1). Black isocontour of $c = 0.5$ represents the boundary of the saltwater and the freshwater zones.

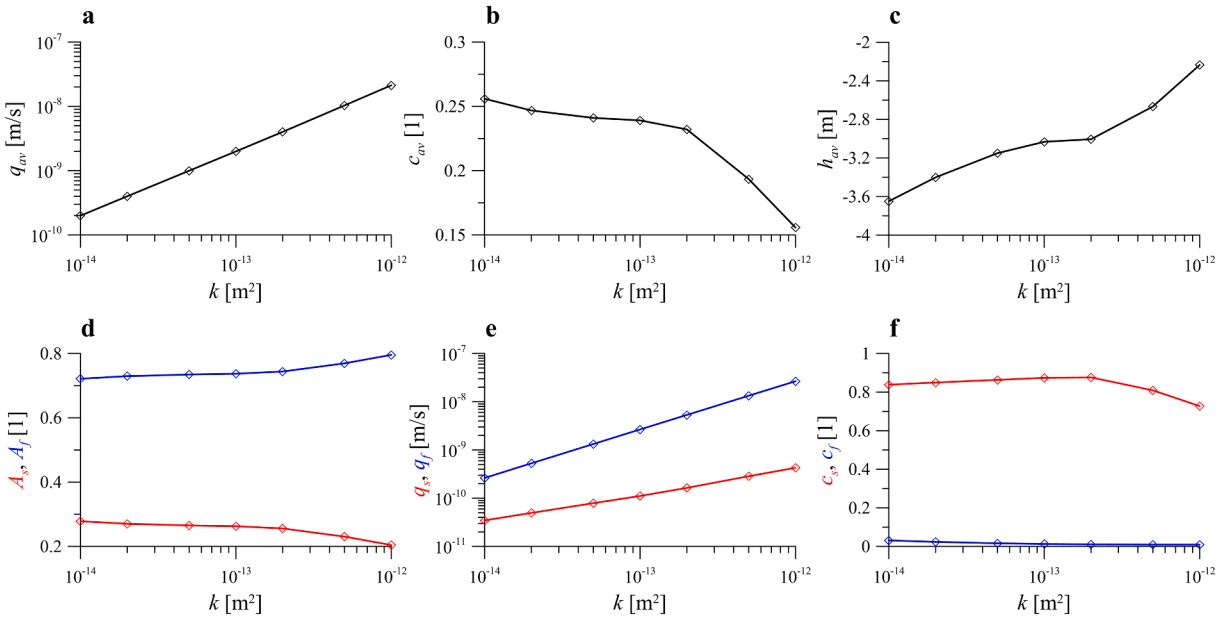

Fig. 6. Stationary solutions of the monitoring parameters plotted against the matrix permeability, k. (a) The average Darcy flux, (b) the average salt concentration and (c) the average hydraulic head. (d) The relative area, (e) the Darcy flux and (f) the concentration averaged for the saltwater (red) and the freshwater (blue) zones.

approximated by an exponential trend. In Eq. (6) γ represents the factor of the permeability decay, that is the ratio of the surface and bottom permeability. Fig. S1 (Supplementary material) illustrates the effect of γ on the concentration field within the interval of γ = 1–100. Increasing γ has a very similar influence on salinity as decreasing permeability in the previous part. When the permeability decreases with depth by a factor of 1–10 (Fig. S1.a–d), a homogenization occurs in the saltwater zone due to the lower Darcy flux in the freshwater zone (Fig. S2.e in Supplementary material) and the reduced diffusion flux across the boundary of the salt- and freshwater zones. The only difference between Fig. 5 and Fig. S1 is that the homogenization evolves not in the whole saltwater dome, but it has a depth-dependence (γ > 1). This process results in a considerable increase in average concentration (Fig. S2.b), the area and the concentration of the saltwater zone (Fig. S2.d and f).

Decreasing permeability with depth by 1–2 orders of magnitude (γ = 10–100) brings forward another phenomenon (Fig. S1.d–g). The Darcy flux decrease with depth is so pronounced that the diffusion approximates the advection in the mass transport, thus a diffusion zone forms between the fresh- and saltwater zones, as well as along the bottom boundary. It enhances the salinity in the freshwater zone (Fig. S2.f). Because of the depth-dependent permeability, the diffusion zone thins upwards, and in the near-surface region, the intense flow effectively erodes the top of the saltwater dome. Consequently, a slight reduction can be observed in the average concentration (Fig. S2.b), the area and the concentration of the saltwater dome (Fig. S2.d and f). Depth-dependent permeability induces a continuous Darcy flux and hydraulic head decrease in the whole basin (Fig. S2.a and c), however, the flow slows down less in the freshwater zone, which occupies the shallower zones of the basin (Fig. S2.e).

3.2.3. *Permeability anisotropy*

The permeability anisotropy coefficient, which is the ratio of the horizontal to vertical permeability, was varied ranging between ε = 1–1000, while the value of the horizontal permeability was fixed, $k_x = 10^{-12}$ m^2. Weakening the vertical permeability leads to slower flow which extends the simulation time. For models, where 2 Myr was not enough to reach the stationary solution, and the variation of the monitoring parameters was very slow, a steady-state solution was calculated from the end of the time-depending solution.

It was found that the anisotropy strongly modifies the shape of the saltwater zone. Fig. 7 displays the stationary solution of the salt concentration at different permeability anisotropies. As the anisotropy increases from ε = 1 to 50 (Fig. 7.a–d), the boundary between the salt- and the freshwater zones changes from convex to concave, since the groundwater flow becomes constrained to shallower zones. Growing the anisotropy beyond the value of ε = 100, the penetration of the regional groundwater flow decreases, and a sluggish layer evolves in the deep part of the basin. In the case of ε = 1000, this sluggish zone becomes thicker (approx. 1.5–2 km). The concentration in the salt layer shows a diffuse pattern indicating that there is no relevant advective mass transport.

Monitoring parameters point out the dichotomy of the effect of anisotropy. As ε increases, the average Darcy flux decreases with an increasing gradient (Fig. 8.a). The change in the morphology of the saltwater dome (ε = 1–50) is reflected in a slight decrease of the average concentration and the relative area of the saline zone (Fig. 8.b and d). Within this interval, the Darcy flux in the saltwater zone is nearly constant. At higher anisotropy values (ε ≥ 50) the topography-driven fresh groundwater does not reach the bottom of the basin, which facilitates the formation of the deep, saline, sluggish, dense layer above the bottom. This thickening layer enhances the average salt content (Fig. 8.b), which results in a relevant head decrease (Fig. 8.c). The size of the saline zone increases (Fig. 8.d), and the Darcy flux decreases steeply (Fig. 8.e). As a result of the appearance of the diffuse transition across the salt- and freshwater boundary, the salt content of the freshwater zone grows (Fig. 8.f).

3.3. *Effect of dispersivity*

Longitudinal dispersivity was raised from the value of the base model, α_L = 0 to 100 m (Fig. 9), meanwhile the transverse dispersivity varied together with α_L as $\alpha_T = \alpha_L/10$. Even though the longitudinal dispersivity is only α_L = 1 m, the concentration distribution within the saline dome becomes more homogeneous (Fig. 9.b). By increasing α_L to 10 m, the salt content is getting higher owing to (1) the enhanced longitudinal dispersion of inner convection within the saltwater zone, and (2) the higher transverse dispersion across the bottom below the saline dome (Fig. 9.a–e). As the dispersivity was increased further (α_L = 10–100 m), the boundary separating the salt- and the freshwater zone thickens due to the incremented transverse dispersion. In addition, a

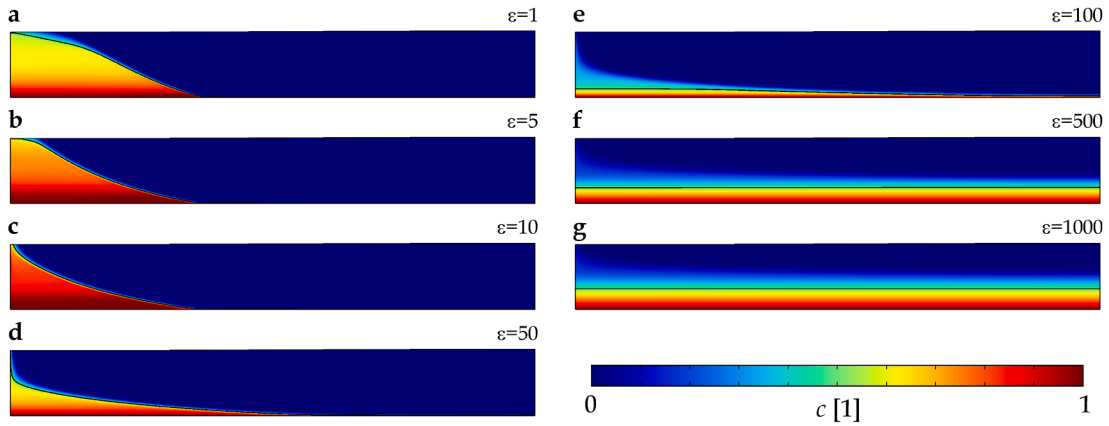

Fig. 7. Stationary solution of salt concentration at different permeability anisotropy, ε = 1–1000. Other parameters are defined in the base model (Table 1). Black isocontour of c = 0.5 represents the boundary of the saltwater and the freshwater zones.

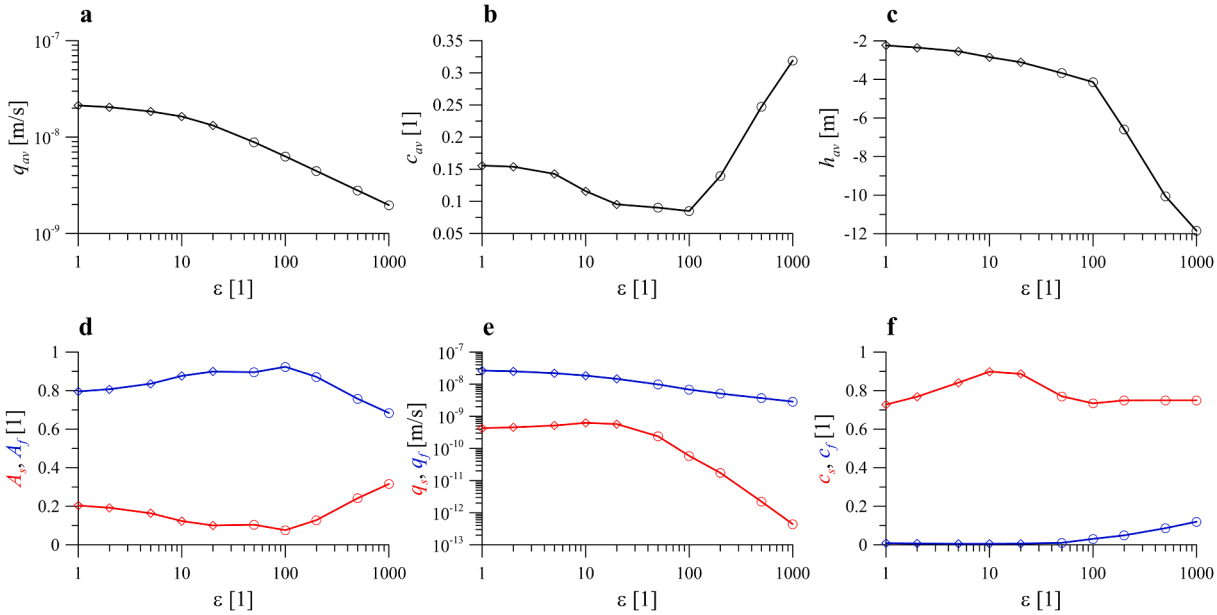

Fig. 8. Stationary solutions of the monitoring parameters plotted against the permeability anisotropy, ε. (a) The average Darcy flux, (b) the average salt concentration and (c) the average hydraulic head. (d) The relative area, (e) the Darcy flux and (f) the concentration averaged for the saltwater (red) and the freshwater (blue) zones. The end of the time-dependent solution is denoted by diamond, the stationary solution computed from the end of the time-dependent solution is denoted by a circle.

thin salty layer evolves along the bottom of the model beneath the freshwater zone. Mechanical dispersion facilitates the solute content mixing both within and between the zones, and consequently, it enhances salt transport. The surface Sherwood number (Weatherill et al., 2004) increases from 146 to 1410 within the range of α_L = 0–100 m.

Fig. 10 quantifies the above-mentioned processes. Within the interval of α_L = 0–10 m, the saltwater zone enlarges from A_s = 20% to 30% (Fig. 10.d), its solute content increases by dispersive mixing (Fig. 10.f), and the flow intensifies due to the stronger linkage between the salt dome and the topography-driven freshwater zone (Fig. 10.e). The broadening salt dome reduces the average Darcy flux of the basin flow by approx. 10% (Fig. 10.a), enhances the average salt content considerably (Fig. 10.b), which results in lower hydraulic heads (Fig. 10.c). When the longitudinal dispersivity is ranged from α_L = 10 to 100 m, there is no such a significant variation in the monitoring parameters. As the transition zone thickens due to the effective transverse dispersion flux (between the salt- and freshwater zones, and along the bottom of the basin), the Darcy flux difference and the solute content difference between the two zones moderate (Fig. 10.e and f).

3.4. *Effect of water table amplitude*

The influence of topography-driven groundwater flow can be directly stimulated by the water table gradient. In the synthetic model, the amplitude of the water table was varied between A = 0 and 500 m to observe the modification of the saltwater zone. In the models where the amplitude was higher than that of the base model (A > 50 m), the regional groundwater flow was intense enough to press the saline dome to the left side (Fig. 11.e–g). The saline zone shrank toward the stagnation point and its density increased to be able to resist the regional freshwater flow. For lower water table amplitudes (A < 50 m) the topography-driven flow weakens, thus the saline zone tends to pervade the deeper part of the basin to form a dense, saline layer (Fig. 11.a–c). It is worth noting when the amplitude is approx. A = 10 m, the topography-driven groundwater flow is weak enough to press the saline dome to the discharge zone, but strong enough to advect the brackish

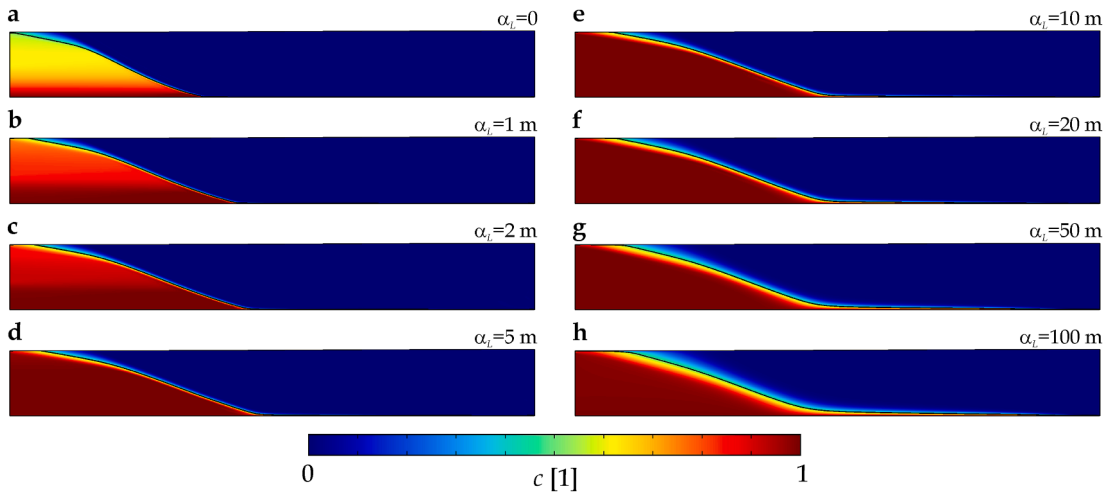

Fig. 9. Stationary solution of salt concentration at different longitudinal dispersivity, α_L = 0–100 m. Transverse dispersivity is $\alpha_T = \alpha_L/10$, other parameters are defined in the base model (Table 1). Black isocontour of $c = 0.5$ represents the boundary of the saltwater and the freshwater zones.

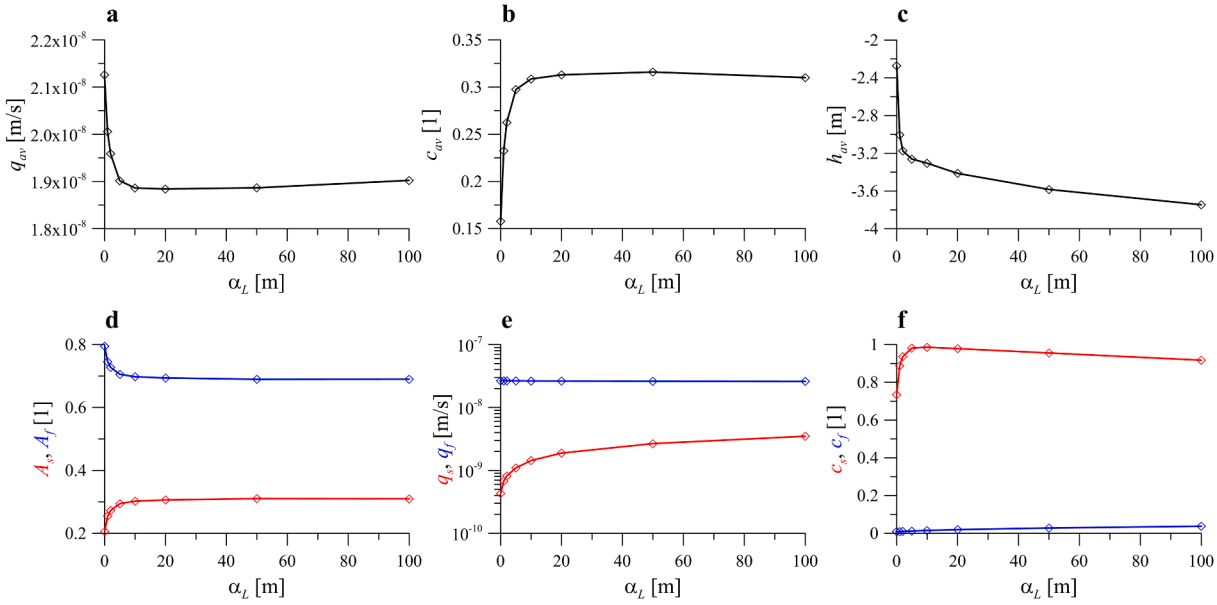

Fig. 10. Stationary solutions of the monitoring parameters plotted against the longitudinal dispersivity, α_L. (a) The average Darcy flux, (b) the average salt concentration and (c) the average hydraulic head. (d) The relative area, (e) the Darcy flux and (f) the concentration averaged for the saltwater (red) and the freshwater (blue) zones.

water from the model (Fig. 11.b). As a result, the size of the saline zone is reduced. At $A = 1$ m, the regional flow is weak, which results in a nearly diffuse density-based layering (Fig. 11.a).

Stationary numerical solutions show a linear relationship between the average Darcy flux and the water table head, following Darcy's law formulated in Eq. (2) (Fig. 12.a). The more intense the regional flow is, the lower the average salt concentration in the basin is noticed (Fig. 12.b), and lower salt content causes higher hydraulic heads (Fig. 12.c). Hydraulic head higher than zero is the consequence of that the area dominated by recharge is enhanced, while the area dominated by discharge is reduced. At $A = 50$ m the relative area of the zone having $h > 0$ is 50.3%, while it is 53.1% at $A = 500$ m. As the water table amplitude decreases, the average head becomes more negative, for the model of $A = 1$ m, only 15.1% of the model domain is characterized by a hydraulic head higher than zero.

Decreasing water table amplitude eventuates in that the Darcy flux is reduced both in the fresh- and the saltwater zone (Fig. 12.e). The flow within the saline zone is slower by 1–2 orders of magnitude. The Darcy flux in the model without water table variation ($A = 0$) tends to zero, therefore it is not displayed in Fig. 12.e. The size of the saline zone increases by weakening the topography-driven flow (A), and it converges to $A_s = A_f = 0.5$ at $A = 0$ (diffuse solution) in Fig. 12.d. However, a local extremum appears in the curves near $A = 10$ m, where a transition exists in the morphology of the saltwater zone, and the saline dome transforms into a deep, saline layer. The salt content of the freshwater zone is practically zero if $A > 50$ m, the regional flow sweeps out the saltwater from the topography-dominated groundwater zone (Fig. 12.f). Since the salt content of the saline zone increases by A, a sharp boundary evolves between the two zones in the absence of mechanical dispersion (Fig. 11.g). On the contrary, reducing A the concentration of the two zones converge to the diffuse solution, $c_s = 0.75$ and $c_f = 0.25$.

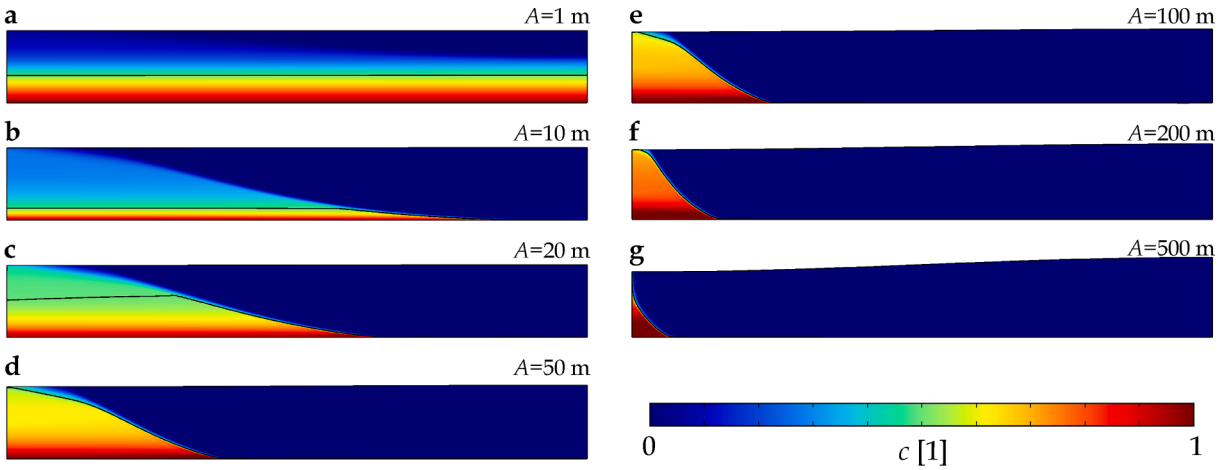

Fig. 11. Stationary solution of salt concentration at different water table amplitudes, $A = 0$–500 m. Other parameters are defined in the base model (Table 1). Black isocontour of $c = 0.5$ represents the boundary of the saltwater and the freshwater zones.

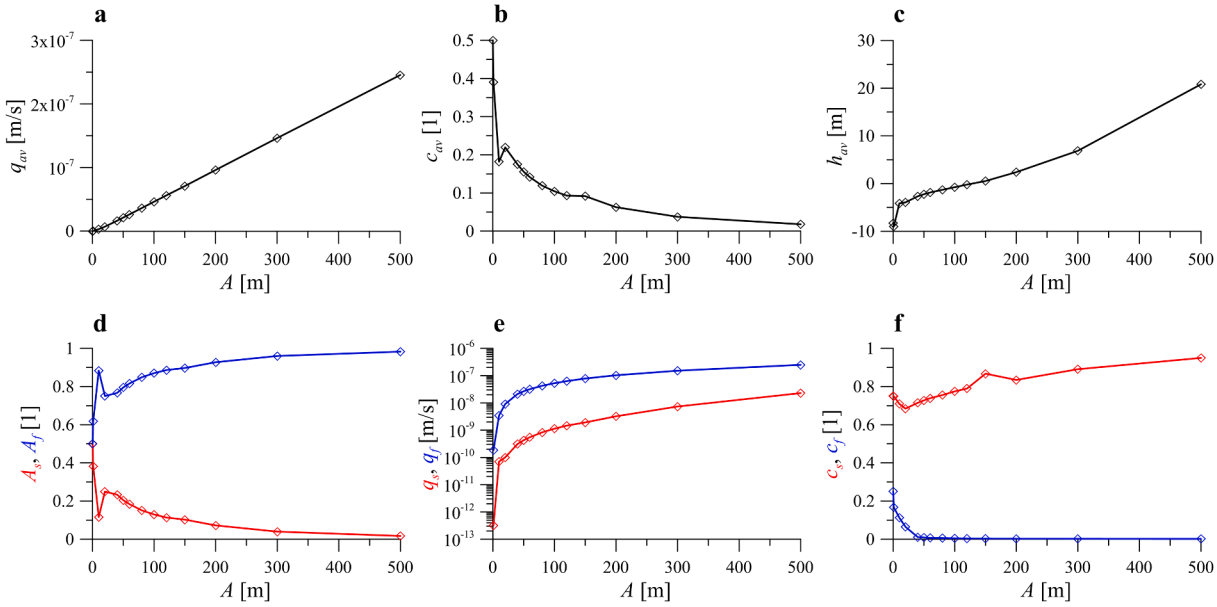

Fig. 12. Stationary solutions of the monitoring parameters plotted against the water table amplitude, A. (a) The average Darcy flux, (b) the average salt concentration and (c) the average hydraulic head. (d) The relative area, (e) the Darcy flux and (f) the concentration averaged for the saltwater (red) and the freshwater (blue) zones. (e) The values of q_s and q_f at $A = 0$ tend to be zero, thus they are not marked in the logarithmic scale.

4. Demonstration in a realistic environment

A two-dimensional section was selected to demonstrate the interaction of topography- and salinity-driven groundwater flows in a real hydrological environment in Hungary. The area was extensively investigated by Mádlné Szőnyi et al. (2018), Mádl-Szőnyi et al. (2019) and Mádlné Szőnyi (2020) studying the geological and structural settings, hydrostratigraphy, examining the hydrocarbon and hydrogeological systems, analysing pressure and salinity data from wells etc. in detail. In addition, a two-dimensional numerical simulation was carried out taking into the consideration only the effect of topography and the advective heat transport (Mádl-Szőnyi et al., 2019). Therefore, in this part, only the most relevant information is summarized, which is necessary to elucidate the background of the numerical flow and transport simulation and time-variation of salinity.

Fig. 13 illustrates the location of the section in the NW part of the Great Hungarian Plain crossing the Gödöllő Hills from SW to NE direction in Hungary. The section length is 48.5 km, the depth of the model varies between 3590 and 3625 m depending on the water table topography. The geology of the area was grouped into five hydrostratigraphic units (HsU) complemented by the original pore fluid content (Table 3): the karstified Triassic carbonate (HsU1); the Eocene limestone (HsU2); the clayey Oligocene aquitard (HsU3); the siliciclastic Miocene aquifer-aquitard group (HsU4) and the undifferentiated Upper Miocene-Pliocene-Quaternary group (HsU5) (Mádlné Szőnyi, 2020). In the hydrostratigraphic division, HsU1 and HsU5 are considered as the main aquifers, and HsU3 represents the main aquitard based on geological and hydrogeological descriptions and evaluation of pumping test data (Rman and Tóth, 2011; Garamhegyi et al., 2020). The hydrostratigraphic section of the study area and the location of faults are originally based on seismic interpretation of MOL Plc. (Mádlné Szőnyi et al., 2013).

The most significant difference between the present model and the model of Mádl-Szőnyi et al. (2019) is that the evolution of the salinity is taken into account here following Eq. (4). Since most hydrostratigraphic units were deposited in a marine environment, we simplified the real

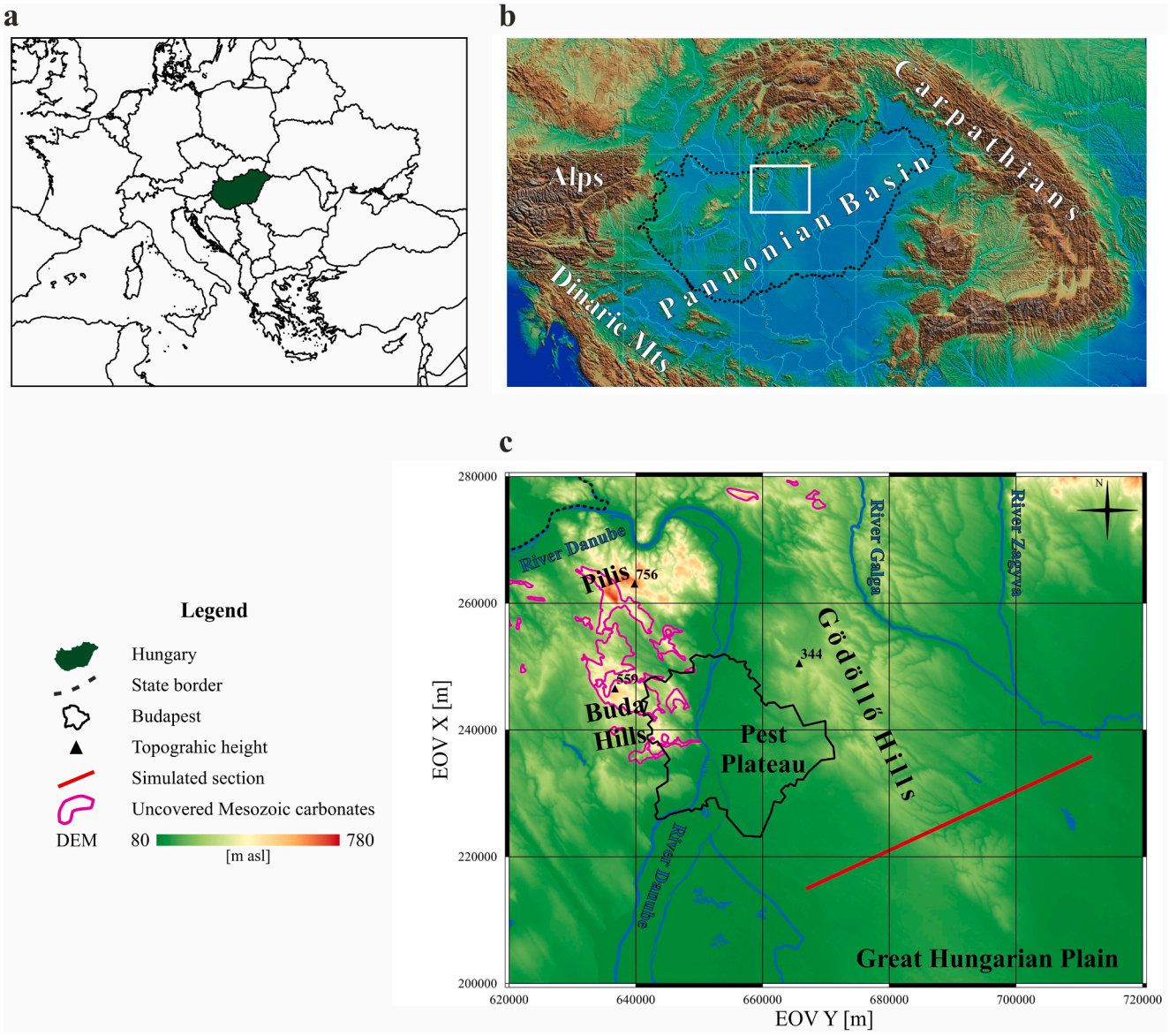

Fig. 13. The location of the study area: (a) Hungary in Europe, (b) the topography of the Pannonian Basin and the broad vicinity of the study area (Horváth et al., 2006) and (c) the topography and the outcrops of Mesozoic carbonates with the simulated hydrogeological cross-section in EOV coordinate system (National Hungarian Grid in meter unit).

Table 3
Description and model parameters of the hydrostratigraphic units, faults based on Mádl-Szőnyi et al. (2019).

Hydrostratigraphic units	Age	Mean depth [m]	Sedimentary environment	Pore fluid	Horizontal hydraulic conductivity [m/s]	Porosity [1]	Anisotropy [1]
HsU5	Upper Miocene-Pliocene-Quaternary	530	undifferentiated siliciclastics	from brackish to meteoric	10^{-5}	0.15	100
HsU4	Miocene	1480	undifferentiated siliciclastic carbonate	marine	10^{-6}	0.08	100
HsU3	Oligocene	1990	deep water shale	marine	10^{-9}	0.05	100
HsU2	Eocene-Oligocene	2430	siliciclastic carbonate with karstification	marine & meteoric	10^{-6}	0.2	100
HsU1	Paleozoic-Triassic-Jurassic	3000	fractured, karstified marine carbonate	marine	10^{-5}	0.2	10
Faults	–	–	–	–	10^{-5}	0.1	1

situation and the initial condition for salt concentration was $c = 1$ in each unit at a relative density difference of $\beta = 3\%$ (TDS of approx. 40,000 mg/l). The boundary conditions for the flow are a linearized surface water table with a maximum elevation of 125 m at $x = 20$ km representing the Gödöllő Hills (Fig. 14.a). Along the left and right boundary of the model the head is fixed at 100 m and 90 m, respectively, showing the flow-through character of the model. The model is closed from below by a no-flow boundary. Boundary conditions for the salt

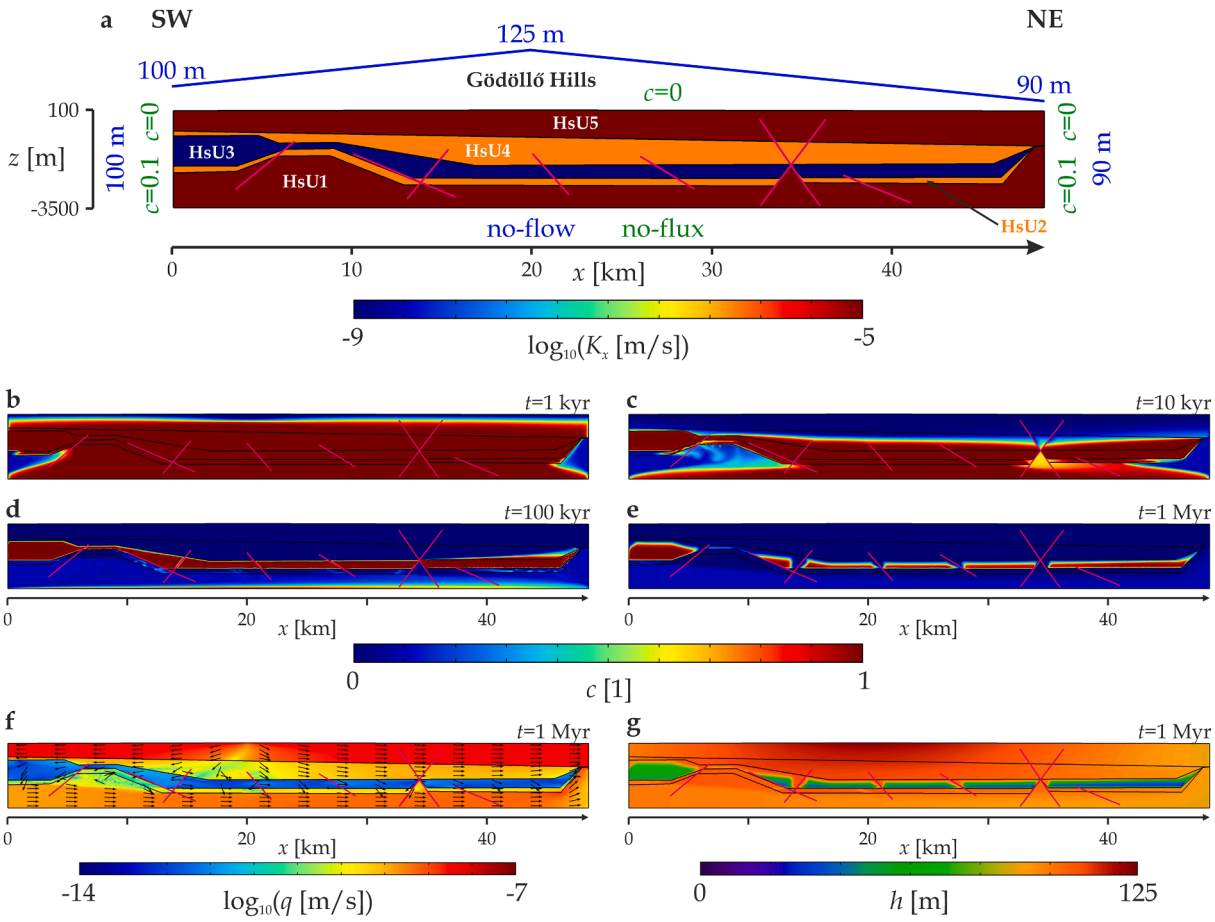

Fig. 14. (a) The horizontal hydraulic conductivity (K_x) of the hydrostratigraphic units and the location of faults (magenta) with the boundary conditions for the flow (blue) and the salt concentration (green). Concentration distribution along the section at (b) $t = 1$ kyr, (c) $t = 10$ kyr, (d) $t = 100$ kyr and (e) $t = 1$ Myr. (f) The Darcy flux magnitude and (g) the hydraulic head field at $t = 1$ Myr. (f) Normalized black arrows illustrate the flow direction. Vertical exaggeration is 1.5.

concentration are $c = 0$ on the surface, knowing that the study area is a recharge zone, while the bottom boundary is no-flux, representing the impervious base rock. Along the side walls $c = 0$ in HsU4 and HsU5, where the freshwater outflow dominates, and $c = 0.1$ in HsU1–HsU3 units, which have no direct connection to meteoric waters. Faults are implicated in the model as domains with an average aperture of 10 m and characterized with hydrogeological parameters listed in Table 3.

Additional modifications were made compared to the model of Mádl-Szőnyi et al. (2019). Mechanical dispersion was introduced due to the coupled topography- and salinity-driven problem. Based on the former synthetic model results, the value of the longitudinal dispersivity was defined as $\alpha_L = 100$ m and the transverse dispersivity was $\alpha_T = 10$ m. In order to handle the effective molecular diffusion in porous medium D_{eff}, the Bruggeman model was used (Wu et al., 2019), that is $D_{eff} = \Phi^{3/2} D_{diff}$. Using additional thermal well hydraulic data, the horizontal hydraulic conductivity of HsU1 and HsU2 was reduced by one order of magnitude. Also, the values of anisotropic coefficients were increased from $\varepsilon = 10$ to 100 in units HsU2–HsU5, where the layered siliciclastic sediments effectively retard the vertical groundwater flow (e.g. Galsa, 1997; Rman and Tóth, 2011; Hoque and Burgess, 2020).

The evolution of the salt concentration is presented for four different time steps up to the maximum simulation time of 1 Myr (Fig. 14.b–e). Only 1 kyr is enough for the meteoric water to displace the saltwater in the upper part of HsU5. After 10 kyr, saltwater is swept out from HsU5 and the upper part of HsU4. Dense, salty plumes descend from the clayey HsU3 aquitard into the karstified HsU1 at $x = 3$–10 km, where the aquitard is the thinnest (Fig. 14.c). The faults at $x \approx 6$ and 34 km, where the salt content decrease appears firstly, facilitate the hydraulic connection between the aquifers above and below HsU3. After 100 kyr HsU4 and HsU5 are fully saturated by freshwater, while HsU1 is saturated by brackish water flowing through this domain from SW to NE (Fig. 14.d). Small-scaled salty downwellings are noticeable in HsU2, directly below the Oligocene aquitard (HsU3). After 1 Myr a considerable part of the original salt content has already been preserved in the lower part of HsU3, however, the salinity of the layer has not been uniform (Fig. 14.e). The concentration is higher in the zones, which are thicker and are far from the hydraulically conductive faults. If the saline water reaches a fault or the boundary of HsU3 by diffusion, it will be effectively advected and displaced by fresh/brackish groundwater. Fig. 14.f emphasizes that HsU4 and HsU5 are dominated by topography-driven meteoric groundwater flow, while HsU1 and HsU2 are prevailed by brackish through-flow. However, the upper and lower units are not perfectly separated, because the two groundwater types communicate through faults and the thin parts of the HsU3 aquitard. Finally, we note that a hydraulic head maximum (120–125 m) can be noticed in the surroundings of the topographic divide, Gödöllő Hills ($x = 20$ km) (Fig. 14g). On the other hand, distinctive head minima appear in the lower part of HsU3 correlating with the salt content. Within these zones, even a 100 m head decrease is present compared to the freshwater zone.

5. Interpretation and discussion

5.1. Synthetic scenarios

Based on the synthetic simulations, it was established that a saltwater zone evolves beneath the discharge zone as a result of a dynamic

equilibrium between the negative buoyancy force of saltwater and the topography-driven fresh groundwater flow. The size and shape of the saline zone depend on the studied parameters. In general, if the effect of salinity becomes dominant, the saltwater zone forms a dense, salty layer in the deeper part of the basin. If the salinity-driven buoyancy prevails against the regional flow, the salt concentration tends to the diffuse distribution without advective solute content transport. This is the case, when the relative density contrast ($\beta \geq 10\%$, Fig. 2.d–g) and the permeability anisotropy ($\varepsilon \geq 100$, Fig. 7.e–g) are enhanced or the water table amplitude is reduced ($A \leq 5$ m, Fig. 11.a–b). However, if the topography-driven groundwater flow becomes dominant, the saltwater zone shrinks, and it is pressed toward the stagnation point beneath the discharge zone. The diffusion from below is not sufficient to maintain an extended saline zone against the regional flow. This solution is obtained from the simulations by decreasing the salinity ($\beta < 1\%$, Fig. 2.a) or by increasing the water table amplitude ($A > 200$ m, Fig. 11.g).

Monitoring parameters quantify the effects of studied parameters on Darcy flux, the salt concentration and the hydraulic head etc. computed for the entire basin and/or the salt- and freshwater zone. Besides, they highlight the modifications in the extent and morphology of the saltwater zone (saline zone to layer at $\varepsilon = 100$, Fig. 8.b–d), or the transition from advection- to diffusion-dominated mass transport system (at $A =$ 10 m, Fig. 12.b and d). Darcy flux values averaged for the different zones indicate that sluggish circulation occurs within the saltwater zone. The flow in the saline zone is slower by approx. 1–2 orders of magnitude, but q_s and q_f seem not to be independent of each other. The diffusion mechanism is supposed to couple these two zones. Near the zone boundaries, the diffusive flux is high due to the large concentration gradient, and the salt content in the saline zone decreases resulting in buoyancy force and upward motion being parallel to the regional groundwater flow (Fig. 3). We note that this weak linkage can be overtaken by small-scale heterogeneities within the saltwater zone, which can lead to more complex inner convection (Fig. S3 in Supplementary material).

In the studied parameter interval, the variation of permeability and dispersivity do not cause relevant modifications in the shape of the saline water zone. It is worth mentioning that qualitatively, the permeability decrease and the dispersivity increase affect the structure of the saline zone in a similar way. First, the salt content increases by homogenization (Fig. 5.a–d and Fig. 9.a–d), then it decreases by thickening the transition between the two zones (Fig. 5.e–g and. Fig. 9.e–h). The latter process can be attributed to the increase of the relative effect of diffusion (reducing the permeability retains the role of advection) and to the amplification of transverse dispersion. Both phenomena strengthen the coupling between the two zones, as it is supported by the fact that the difference between q_f and q_s decreases from 2 to 1 orders of magnitude (Fig. 6.e and Fig. 10.e). The effect of the permeability decreasing exponentially with depth is very similar to the case of permeability decrease, but its influence weakens toward the surface.

Dimensionless numbers facilitate the simultaneous interpretation of the effects of different model parameters on the behavior of the groundwater flow system. Sherwood number (*Sh*) describes the ratio of the surface concentration flux and the concentration flux due to purely diffusion. It means that the larger the value of *Sh*, the stronger the role of advection/convection in the solute transport. Péclet number (*Pe*) expresses the convective transport (i.e. q_{av}, the average Darcy flux in simulations) compared to diffusion and dispersive solute transport,

$$Pe = \frac{q_{av} d}{D_{diff} + \alpha_L q_{av}}. \tag{7}$$

Both the diffusive and dispersive fluxes are used in the denominator since both hinder the convection (e.g. Simmons and Narayan, 1997).

Fig. 15.a shows the Sherwood number plotted against the Péclet number for each synthetic simulation. Increasing salinity (β) retains the flow slightly and reduces the surface solute flux by almost one order of magnitude. Decreasing permeability in the homogeneous (*k*), the depth-dependent (γ) and the anisotropic (ε) models slow down the flow and lessens the surface concentration flux. When the effective permeability decreases with depth (γ, ε), where the salt content is higher, a reduction in *Sh* is more pronounced. Although the dispersivity (α_L) decreases *Pe* (by enhancing the denominator of (7)), *Sh* increases owing to the stronger coupling between the salt- and freshwater zones by higher transverse dispersion. Higher water table amplitude (*A*) intensifies the advective transport and raises the surface concentration flux. While lower water table amplitude decreases both *Pe* and *Sh*, and drives the system toward the thin saline layer and then toward the diffusion state. In the most numerical solutions, a dense, sluggish, saline dome forms beneath the discharge zone, but decreasing the water table amplitude (*A*) or increasing permeability anisotropy (ε) and salinity (β), the system transforms into a thin layer or a diffusion regime (solid symbols).

Szijártó et al. (2019) defined a modified Péclet number to separate the effect of thermal buoyancy from the total convective Darcy flux in synthetic groundwater flow models driven by mixed thermal convection. In this paper, we reinterpreted the former definition, because (1) advection competes with molecular diffusion and mechanical dispersion (instead of thermal diffusion), and (2) the haline convection retards the flow in the studied models. Thus, the modified Péclet number is

$$Pe^* = \frac{(q_{adv} - q_{av})d}{D_{diff} + \alpha_L q_{av}} \tag{8}$$

using the difference between the advective (q_{adv}) and the total convective (q_{av}) Darcy flux. Advective Darcy flux was calculated for each simulation at $\beta = 0$, that is the negative buoyancy force of salinity was

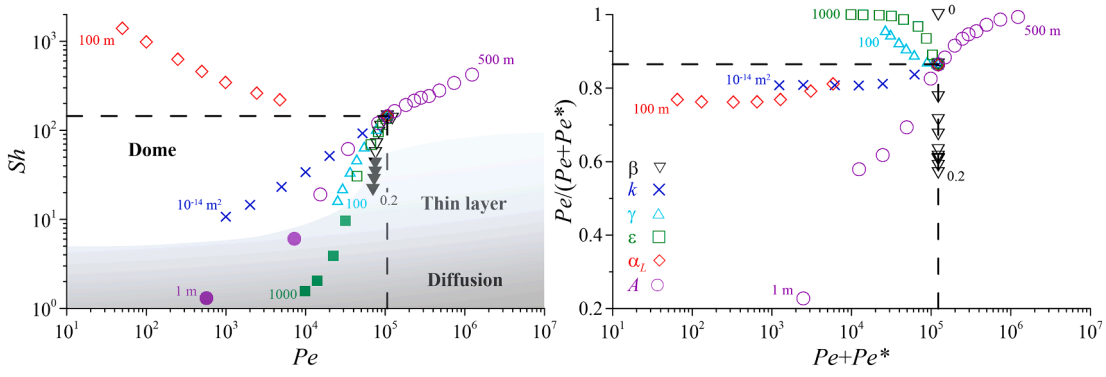

Fig. 15. (a) Sherwood number (*Sh*) plotted against the Péclet number (*Pe*) calculated for each synthetic simulation. The saline layer/diffusion regime is separated from the saline dome regime by shading. (b) Non-dimensional numbers obtained from the Péclet number and the modified Péclet number (*Pe**) calculated for each synthetic simulation. The studied model parameters are denoted by different symbols in (b) and their extremums are labelled. The intersection of dashed lines shows the base model (Table 1).

neglected.

The relation between the topography-driven and the buoyancy-driven groundwater flow is elucidated in Fig. 15.b, where $Pe + Pe^*$ is proportional to the advective Darcy flux and $Pe/(Pe + Pe^*)$ shows the ratio of the total convective and advective Darcy flux (see Eq. (7) and (8)). When the salinity does not influence the flow ($\beta = 0$), the advective (q_{adv}) and convective flux (q_{av}) are identical, $Pe/(Pe + Pe^*) = 1$. The increase in salinity retains the regional groundwater flow, e.g. the convective Darcy flux at a value of $\beta = 0.2$ is reduced by 43%. The decrease of permeability in a homogeneous medium (k) and the increase in mechanical dispersion (α_L) similarly affect the convective flux (see Figs. 5 and 9). Decrease in k and increase in α_L considerably reduce the advective transport compared to diffusion and dispersion ($Pe + Pe^*$), respectively, but these effects moderate the convective flow relative to the base model by only some percent. Effective permeability decreasing with depth (γ, ε) slows down the flow and lessens the role of salinity-induced buoyancy force, as $Pe/(Pe + Pe^*)$ tends to 1. Increasing the water table amplitude (A) strengthens the advective flux and weakens the influence of salinity on the flow. On the other hand, decreasing water table amplitude accentuates the negative buoyancy force, as, for instance, the convective flux at $A = 1$ m is reduced to 23%.

Zhang et al. (2020b) noted that the increase of salinity retards the nested groundwater flow intensity — analogously to our findings —, although their hierarchical synthetic models have different boundary conditions. Qualitatively, a similar brine zone with counter-rotating inner convection forms beneath playas, as an interaction between the freshwater infiltration in the surrounding mountains and the redissolution of evaporites in playas both on regional (Duffy and Al-Hassan, 1988) and on a local scale (Hamann et al., 2015). However, in these models, the saltwater recharge across the surface destabilizes the system and stimulates the groundwater flow, while in our models, the salt transport occurs from below, which stabilizes the system and hinders the groundwater flow. At the same time, the dispersive flux through the boundary of the salt- and freshwater zones appears in both simulations. The transverse dispersion between the two zones enhances the coupling between the flow systems by decoupling the flow from the salt transport, as was concluded by Wen et al. (2018), who investigated the role of dispersion on CO_2 storage in deep saline aquifers.

In an examined realistic hydrogeological situation ($\beta = 2.5\%$, $k_x = 10^{-12}$ m^2, $\varepsilon = 100$, $\alpha_L = 100$ m and $A = 50$ m) a thin saline layer (approx. 17,500–35,000 mg/l) formed due to the high anisotropy coefficient and it occupied the lower 7.6% of the basin (lower 380 m). The average TDS content of the saline layer and the topography-driven upper zone was 26,100 mg/l and 1,240 mg/l, respectively. The brackish character of the upper zone is explained by the large value of transverse dispersivity, $\alpha_T = 10$ m, which enhanced the salinity flux into the freshwater zone. The maximum TDS content near the surface approximates only 630 mg/l in the leftmost part of the discharge zone, however, this value reaches 4000 mg/l at a depth of 200 m, which can seriously deteriorate the quality of the water in case of drinking and irrigation utilization. The Darcy flux in the upper zone ($q_f \approx 6.8 \cdot 10^{-9}$ m/s) is higher than that in the saline, sluggish layer by a factor of approx. 110. The average water density in the saline water layer is 1018 kg/m^3 resulting in a 50 m hydraulic head decrease in the entire layer.

5.2. Realistic scenario

Numerical modelling of the studied hydrogeological section illustrates that the high salt content trapped in the clayey Oligocene aquitard (HsU3) can survive over 1 Myr. Based on samples of hydrocarbon and thermal wells, high TDS content in the Oligocene aquitard (30,000–50,000 mg/l) and brackish pore water observed in Triassic carbonates (1,000–10,000 mg/l) (Mádl-Szőnyi et al., 2019) agree with the numerical model results (Fig. 14.e). The elevated TDS content explains the hydraulic head deficit measured in HsU3, and it is in harmony with the finding, that the thicker HsU3, the lower the hydraulic head. However, higher salt content cannot elucidate the "underpressure" (Mádl-Szőnyi et al., 2015), which might be the result of decompaction and insufficient groundwater replenishment due to the uplifting of Gödöllő Hills, which started 3–4 Myr ago (Ruszkiczay-Rüdiger et al., 2007).

During the last 3–4 Myr, Gödöllő Hills became a topographic divide, which facilitated the significance of a topography-driven groundwater flow system. Since the entire section is a recharge area, the upper Neogene and Quaternary units (HsU4 and HsU5) are characterized by low TDS. Based on data evaluation, the fractured and confined Triassic carbonate is likely to be in connection with unconfined carbonate on the western side of Danube River (Fig. 13.c), so it is part of the Buda Thermal Karst (BTK) system (Mádl-Szőnyi and Tóth, 2015; Szijártó et al., 2021). However, the connection and isolation are tectonically influenced, thus it can differ from place to place (Mádlné Szőnyi, 2020). Brackish pore water in HsU1 and HsU2 can be the consequence of the meteoric water infiltration in the unconfined part of BTK, the hydraulic connection between the unconfined and confined carbonates and the weak saltwater leakage from HsU3. Based on the numerical simulation, the linkage between the topography-driven fresh groundwater (HsU4 and HsU5) and the compositionally mixed brackish karst water (HsU1 and HsU2) is plausible through faults and the thinnest parts of the Oligocene aquitard (HsU3).

These simulations, like each numerical or conceptual model, include simplifications and have limitations, which can modify the outcomes. (1) One of them is that source/sink terms (precipitation and dissolution of salts (e.g. Vásquez et al., 2013; Hamann et al., 2015), evaporite formation etc.) are not built into the simulations, however, the exit of the salt content is allowed through the upper boundary of the synthetic model by diffusion. However, it is supposed that these local-scale processes cannot considerably change the received basin-scale flow pattern. (2) Although equivalent porous media (EPM) approximation can be accepted in the karstified carbonates on basin-scale (e.g. Long et al., 1982; Scanlon et al., 2003; Mádl-Szőnyi and Tóth, 2015), the effect of relevant hydraulically conductive faults was taken into account (Berre et al., 2019). (3) For the sake of simplicity, the effect of thermal buoyancy was neglected in the simulations, which might be another important factor in deep, karstified, basin-scale carbonate systems (e.g. Havril et al., 2016; Szijártó et al., 2019, 2021). However, a recent study showed that in the presence of topography-driven groundwater flow advective heat transport exists, but free thermal convection might occur only at higher Rayleigh numbers (Szijártó et al. 2019). For the purposes of this paper, omittance of buoyancy due to temperature differences can be an acceptable assumption. The fully coupled solutions (topography plus salinity plus temperature) indicate a plausible perspective of further simulations. Nevertheless, a preliminary simulation was completed along the hydrogeological section crossing Gödöllő Hills in order to flash the process of topothermohaline convection, where the flow pattern and the salt concentration is controlled by both the water table topography and the buoyancy force due to the temperature and the salinity variation (Supplementary material). As a working hypothesis for further simulations, it can be established that owing to the elevated geothermal gradient characterizing the area, thermal convection formed in the deep, partly confined karstified aquifers (HSU1 and HSU2), which intensified the flow, strengthened the hydrodynamic connection between the upper (HSU4 and HSU5) and lower aquifers, and facilitated the saltwater drainage from the clayey Oligocene aquitard (HSU3) (Fig. S4 in Supplementary material). (4) In both the synthetic simulations and the case study, the upper boundary condition for the flow was a simple cosinusoid or a linear hydraulic head. However, local variations in the topography and the water table can disturb the flow pattern and the salinity field, as well. A hierarchically nested groundwater system could induce a more complex distribution of the salt concentration and the temperature (Zhang et al., 2020b; An et al., 2015). In general, higher salinity and surface heat flux are expected in the regional discharge area rather than in local discharge/recharge areas. The lowest salinity and

heat flux are probable in regional recharge zones. Nonetheless, the formation of time-dependent thermal buoyancy, which strongly depends on the physical and geometrical model parameters (Szijártó et al., 2019), is able to modulate or even overwrite the above-mentioned simplified consideration resulting in a complex nested system where the flow, the salinity and the heat vary in time and space.

6. Conclusions

Interaction of topography- and salinity-driven groundwater flow was systematically investigated in synthetic two-dimensional, basin-scale numerical models and then in a realistic scenario based on the siliciclastic-carbonate basin in Hungary.

It was established in the synthetic analyses, that the effect of increasing water density due to salinity and decreasing water table amplitude on the saltwater distribution is similar. The first enhances the buoyancy-driven free convection, while the second reduces the topography-driven forced convection. Thus, the numerical solutions trend from a topography-dominated regional freshwater system towards a diffusion-dominated layered system. The increase of permeability anisotropy shows similar progress towards the formation of a dense, saline layer in the deeper part of the basin. In the studied parameter domain, both the decrease of permeability and the increase of dispersivity extinguish the relative role of advection by enhancing the diffusion or dispersion, respectively. The two phenomena strengthen the coupling between the fresh- and saltwater zone.

Based on the synthetic simulation set, the coupled topography- and salinity-driven model was applied along a 2D hydrogeological section in Hungary. After 100 kyr, the original marine pore water is outplaced from both the upper siliciclastic aquifers by topography-driven meteoric freshwater and the lower karstified carbonates by the brackish groundwater through-flow. However, the marine-origin pore water in the middle aquitard can survive over 1 Myr resulting in a significant head minimum. The connection between the upper and lower pervious units are revealed by the presence of conductive faults, while the connection between the clayey cover and confined carbonates is represented by dense, saline finger-like downwellings.

The current study improves the understanding of the interaction between the topography-driven forced and the salinity-driven free convection, especially in basin-scale groundwater flow systems. On the one hand, the sensitivity analysis of the synthetic models highlights the role of the most important model parameters influencing the coupled flow system. On the other hand, the phenomenon of mixed convection was investigated and proved along a simplified 2D hydrogeological section in Hungary to demonstrate the mixing of fresh, brackish and saline water. Nevertheless, the combined topography- and salinity-driven groundwater flow plays an important role in the Atacama salt flat aquifer, Chile (Tejeda et al., 2003; Vásquez et al., 2013), in the surroundings of playas in Pilot Valley, USA (Duffy and Al-Hassan, 1988; Fan et al., 1997), below saline disposal basins in the Murray–Darling Basin, Australia (Simmons and Narayan, 1997), in the salt accumulation in the beach of Bon Secour National Wildlife Refuge, USA (Geng and Boufadel, 2015) etc. Therefore, the results of the study can be used with the necessary adaptations in further terrestrial hydrogeological environments as well.

CRediT authorship contribution statement

Attila Galsa: Methodology, Validation, Investigation, Writing – original draft, Writing – review & editing. **Ádám Tóth:** Data curation, Supervision, Writing – review & editing, Funding acquisition. **Márk Szijártó:** Visualization, Supervision, Writing – review & editing, Funding acquisition. **Daniele Pedretti:** Supervision, Funding acquisition. **Judit Mádl-Szőnyi:** Data curation, Conceptualization, Writing – review & editing, Supervision, Funding acquisition.

Declaration of Competing Interest

The authors declare that they have no known competing financial interests or personal relationships that could have appeared to influence the work reported in this paper.

Acknowledgements

Authors are grateful to the anonymous reviewers for the instructive comments and inspiring suggestions. This research is part of a project that has received funding from the European Union's Horizon 2020 research and innovation program under grant agreement No 810980. The project was supported by the ÚNKP-19-3 and ÚNKP-19-4 New National Excellence Program of the Ministry for Innovation and Technology, by the Hungarian Scientific Research Fund (K 129279), by the János Bolyai Research Scholarship of the Hungarian Academy of Sciences and by the ÚNKP-21-4 New National Excellence Program of the Ministry for Innovation and Technology from the source of the National Research, Development and Innovation Fund. The paper was prepared with the professional support of the Doctoral Student Scholarship Program of the Co-operative Doctoral Program of the Ministry of Innovation and Technology financed from the National Research, Development and Innovation Fund.

Appendix A. Supplementary data

Supplementary data to this article can be found online at https://doi.org/10.1016/j.jhydrol.2022.127695.

References

An, R., Jiang, X.-W., Wang, J.-Z., Wan, L., Wang, X.-S., Li, H., 2015. A theoretical analysis of basin-scale groundwater temperature distribution. Hydrogeol. J. 23 (2), 397–404. https://doi.org/10.1007/s10040-014-1197-y.

Barlow, P.M., Reichard, E.G., 2010. Saltwater intrusion in coastal regions of North America. Hydrogeol. J. 18, 247–260. https://doi.org/10.1007/s10040-009-0514-3.

Berre, I., Doster, F., Keilegavlen, E., 2019. Flow in fractured porous media: A review of conceptual models and discretization approaches. Transp. Porous Media 130, 215–236. https://doi.org/10.1007/s11242-018-1171-6.

Cirpka, O.A., Chiogna, G., Rolle, M., Bellin, A., 2015. Transverse mixing in three-dimensional nonstationary anisotropic heterogeneous porous media. Water Resour. Res. 51, 241–260. https://doi.org/10.1002/2014WR015331.

De Paola, F., Giugni, M., Topa, M.E., Bucchignani, E., 2014. Intensity-Duration-Frequency (IDF) rainfall curves, for data series and climate projection in African cities. SpringerPlus 3, 133. https://doi.org/10.1186/2193-1801-3-133.

Delgado, J.M.P.Q., 2012. Heat and Mass Transfer in Porous Media. Springer, Berlin, Heidelberg, p. 266.

Deming, D., 2002. Introduction to Hydrogeology. McGraw Hill, New York, pp. 480, ISBN-10: 0072326220.

Domenico, P.A., Palciauskas, V.V., 1973. Theoretical analysis of forced convective heat transfer in regional ground-water flow. GSA Bull. 84 (12), 3803–3814. https://doi.org/10.1130/0016-7606.

Dublyansky, Y.V., 1995. Speleogenetic history of the Hungarian hydrothermal karst. Environ. Geol. 25, 24–35. https://doi.org/10.1007/BF01061827.

Duffy, C.J., Al-Hassan, S., 1988. Groundwater circulation in a closed desert basin: topographic scaling and climatic forcing. Water Resour. Res. 24 (10), 1675–1688. https://doi.org/10.1029/WR024i010p01675.

Ehrenberg, S.N., Nadeau, P.H., 2005. Sandstone vs. carbonate petroleum reservoirs: A global perspective on porosity-depth and porosity-permeability relationships. AAPG Bull. 89 (4), 435–445. https://doi.org/10.1306/11230404071.

Fan, Y., Duffy, C.J., Oliver Jr, D.S., 1997. Density-driven groundwater flow in closed desert basins: field investigations and numerical experiments. J. Hydrology 196, 139–184. https://doi.org/10.1016/S0022-1694(96)03292-1.

Galsa, A., 1997. Modelling of groundwater flow along a section in the Great Hungarian Plain using hydraulic heads measured in wells (in Hungarian with English abstract). Magyar Geofizika 38 (4), 245–256. http://epa.oszk.hu/03400/03436/00151/pdf/EPA03436_magyar_geofizika_1997_04_245-256.pdf.

Gao, G., Zhan, H., Feng, S., Fu, B., Huang, G., 2012. A mobile–immobile model with an asymptotic scale-dependent dispersion function. J. Hydrology 424–425, 172–183. https://doi.org/10.1016/j.jhydrol.2011.12.041.

Garamhegyi, T., Székely, F., Carrillo-Rivera, J.J., Mádl-Szőnyi, J., 2020. Revision of archive recovery tests using analytical and numerical methods on thermal water wells in sandstone and fractured carbonate aquifers in the vicinity of Budapest. Hungary. Environmental Earth Science. 79, 129. https://doi.org/10.1007/s12665-020-8835-6.

García-Gil, A., Vázquez-Suñé, E., Ayora, C., Tore, C., Henríquez, Á., Yáñez, J., 2019. Impacts of the transient skin effect during brine extraction operations in a crystalline halite aquifer, J. Hydrology, 577, paper: 123912, 10.1016/j.jhydrol.2019.123912.
Gelhar, L.W., Welty, C., Rehfeldt, K.R., 1992. A critical review of data on field-scale dispersion in aquifers. Water Resour. Res. 28 (7), 1955–1974. https://doi.org/10.1029/92WR00607.
Geng, X., Boufadel, M.C., 2015. Impacts of evaporation on subsurface flow and salt accumulation in a tidally influenced beach. Water Resour. Res. 51, 5547–5565. https://doi.org/10.1002/2015WR016886.
Hamann, E., Post, V., Kohfahl, C., Prommer, H., Simmons, C.T., 2015. Numerical investigation of coupled density-driven flow and hydrogeochemical processes below playas. Water Resour. Res. 51, 9338–9352. https://doi.org/10.1002/2015WR017833.
Havril, T., Molson, J.W., Mádl-Szőnyi, J., 2016. Evolution of fluid flow and heat distribution over geological time scales at the margin of unconfined and confined carbonate sequences - A numerical investigation based on the Buda Thermal Karst analogue. Mar. Pet. Geol. 78, 738–749. https://doi.org/10.1016/j.marpetgeo.2016.10.001.
Havril, T., Tóth, Á., Molson, J.W., Galsa, A., Mádl-Szőnyi, J., 2018. Impacts of predicted climate change on groundwater flow systems: Can wetlands disappear due to recharge reduction? J. Hydrol. 563, 1169–1180. https://doi.org/10.1016/j.jhydrol.2017.09.020.
He, Z., Ding, Q., Wo, Y., Zhang, J., Fan, M., Yue, X., 2017. Experiment of carbonate dissolution: implication for high quality carbonate reservoir formation in deep and ultradeep basins. Geofluids, 2017, paper: 8439259, 10.1155/2017/8439259.
Herbert, E.R., Boon, P., Burgin, A.J., Neubauer, S.C., Franklin, R.B., Ardón, M., Hopfensperger, K.N., Lamers, L.P.M., Gell, P., 2015. A global perspective on wetland salinization: ecological consequences of a growing threat to freshwater wetlands. Ecosphere 6 (10), paper: 206. https://doi.org/10.1890/ES14-00534.1.
Hoque, M.A., Burgess, W.G., 2020. Representing heterogeneity of fluvio-deltaic aquifers in models of groundwater flow and solute transport: A multi-model investigation in the Bengal Basin. J. Hydrology, 590, paper: 125507, 10.1016/j.jhydrol.2020.125507.
Horváth, F., Bada, G., Windhoffer, G., Csontos, L., Dombrádi, E., Dövényi, P., Fodor, L., Grenerczy, G.y., Síkhegyi, F., Szafián, P., Székely, B., Timár, G., Tóth, L., Tóth, T., 2006. Atlas of the present-day geodynamics of the Pannonian basin: Euroconform maps with explanatory text (in Hungarian with English abstract). Magyar Geofizika 47 (4), 133–137. http://epa.niif.hu/03400/03436/00186/pdf/EPA03436_magyar_geofizika_2006_04_133-137.pdf.
Hussain, M.S., Abd-Elhamid, H.F., Javadi, A.A., Sherif, M.M., 2019. Management of Seawater Intrusion in Coastal Aquifers: A Review. Water, 11 (12), paper: 2467, 10.3390/w11122467.
Jalali, M., 2007. Salinization of groundwater in arid and semi-arid zones: an example from Tajarak, western Iran. Environ. Geol. 52, 1133–1149. https://doi.org/10.1007/s00254-006-0551-3.
Jiang, X-W., Wan, L., Wang, X-S., Ge, S., Liu, J., 2009. Effect of exponential decay in hydraulic conductivity with depth on regional groundwater flow. Geophys. Res. Lett., 36 (24), paper: L24402, 10.1029/2009GL041251.
Jiang, X-W., Wang, X-S., Wan, L., Ge, S., 2011. An analytical study on stagnation points in nested flow systems in basins with depth-decaying hydraulic conductivity. Water Resour. Res., 47 (1), paper: W01512, 10.1029/2010WR009346.
Kambesis, P.N., Coke, J.G., 2013. Overview of the Controls on Eogenetic Cave and Karst Development in Quintana Roo, Mexico. In: Coastal Karst Landforms (ed. Lace, M.J., Mylroie, J.E.). Springer, Dordrecht, 347–373, ISBN: 978-94-007-5016-6, 10.1007/978-94-007-5016-6_16.
Karaki, N.A., Fiaschi, S., Paenen, K., Al-Awabdeh, M., Closson, D., 2019. Exposure of tourism development to salt karst hazards along the Jordanian Dead Sea shore. Hydrol. Earth Syst. Sci. 23, 2111–2127. https://doi.org/10.5194/hess-23-2111-2019.
Kesler, S.E., Gruber, P.W., Medina, P.A:, Keoleian, G.A., Everson, M.P., Wallington, T.J., 2012. Global lithium resources: Relative importance of pegmatite, brine and other deposits. Ore Geol. Rev., 48, 55–69, 10.1016/j.oregeorev.2012.05.006.
Konikow, L.F., Akhavan, M., Langevin, C.D., Michael, H.A., Sawyer, A.H., 2013. Seawater circulation in sediments driven by interactions between seabed topography and fluid density. Water Resour. Res. 49, 1386–1399. https://doi.org/10.1002/wrcr.20121.
Kreyns, P., Geng, X., Michael, H.A., 2020. The influence of connected heterogeneity on groundwater flow and salinity distributions in coastal volcanic aquifers. J. Hydrology, 586, paper: 124863, 10.1016/j.jhydrol.2020.124863.
Liu, R., Li, B., Jiang, Y., Huang, N., 2016. Review: Mathematical expressions for estimating equivalent permeability of rock fracture networks. Hydrogeol. J. 24, 1623–1649. https://doi.org/10.1007/s10040-016-1441-8.
Long, J.C.S., Remer, J.S., Wilson, C.R., Witherspoon, P.A., 1982. Porous media equivalents for networks of discontinuous fractures. Water Resour. Res. 18 (3), 645–658. https://doi.org/10.1029/WR018i003p00645.
Mádlné Szőnyi, J., 2020. Pattern of groundwater flow at the boundary of unconfined and confined carbonate systems on the example of Buda Thermal Karst and its surroundings (in Hungarian). DSc Thesis, pp. 150, https://scholar.google.com/scholar?q=Pattern%20of%20Groundwater%20Flow%20at%20the%20Boundary%20of%20Unconfined%20and%20Confined%20Carbonate%20Systems%20on%20the%20Example%20of%20Buda%20Thermal%20Karst%20and%20its%20Surroundings.
Mádlné Szőnyi, J., Czauner, B., Erőss, A., Simon, S., 2013. Karbonátos és Csatlakozó Üledékes Medenceterületek Fluidumdinamikai Összefüggéseinek Vizsgálata a Szénhidrogén Kutatás Hatékonyságának Javítása Érdekében a Paleogén-medencében – Zárójelentés. Investigation of fluid-dynamic connection of carbonate and adjoining basin in hydrocarbon exploration purposes – Final Report. Hungarian Oil Company, Budapest.
Mádlné Szőnyi, J., Erőss, A., Havril, T., Poros, Zs., Győri, O., Tóth, Á., Csoma, A., Ronchi, P., Mindszenty, A., 2018. Fluids, flow systems and their minerological imprints in the Buda Thermal Karst (in Hungarian with English abstract). Földtani Közlöny, 148 (2), 75–96, 10.23928/foldt.kozl.2018.148.1.75.
Mádl-Szőnyi, J., Czauner, B., Iván, V., Tóth, Á., Simon, S.z., Erőss, A., Bodor, P., Havril, T., Boncz, L., Sőreg, V., 2019. Confined carbonates? – regional-scale hydraulic interaction or isolation? Mar. Pet. Geol. 107, 591–612. https://doi.org/10.1016/j.marpetgeo.2017.06.006.
Mádl-Szőnyi, J., Pulay, E., Tóth, Á., Bodor, P., 2015. Regional underpressure: a factor of uncertainty in the geothermal exploration of deep carbonates, Gödöllő Region, Hungary. Environ. Earth Sci. 74 (12), 7523–7538. https://doi.org/10.1007/s12665-015-4608-z.
Mádl-Szőnyi, J., Tóth, Á., 2015. Basin-scale conceptual groundwater flow model for an unconfined and confined thick carbonate region. Hydrogeol. J. 23, 1359–1380. https://doi.org/10.1007/s10040-015-1274-x.
Marazuela, M.A., Vázquez-Suñé, E., Custodio, E., Palma, T., García-Gil, A., Ayora, C., 2018. 3D mapping, hydrodynamics and modelling of the freshwater-brine mixing zone in salt flats similar to the Salar de Atacama (Chile). J. Hydrology 561, 223–235. https://doi.org/10.1016/j.jhydrol.2018.04.010.
McFarlane, D.J., George, R.J., Barrett-Lennard, E.G., Gilfedder, M., 2017. Salinity in dryland agricultural systems: Challenges and opportunities. In: Innovations in Dryland Agriculture (ed. Farooq, M., Siddique, K.H.M.). Springer International Publishing, 521–547, ISBN: 978-3-319-47928-6, 10.1007/978-3-319-47928-6_19.
Nield, D.A., 1968. Onset of thermohaline convection in a porous medium. Water Resour. Res. 4 (3), 553–560. https://doi.org/10.1029/WR004i003p00553.
Nield, D.A., Bejan, A., 2017. Convection in Porous Media, 5th ed. Springer Int, p. 988.
Oz, I., Eyal, S., Yoseph, Y., Ittai, G., Elad, L., Haim, G., 2016. Salt dissolution and sinkhole formation: Results of laboratory experiments. J. Geophys. Res. Earth Surf. 121, 1746–1762. https://doi.org/10.1002/2016JF003902.
Payen, S., Basset-Mens, C., Núñez, M., Follain, S., Grünberger, O., Marlet, S., Perret, S., Roux, P., 2016. Salinisation impacts in life cycle assessment: a review of challenges and options towards their consistent integration. Int. J. Life Cycle Assess. 21, 577–594. https://doi.org/10.1007/s11367-016-1040-x.
Pedretti, D., Russian, A., Sanchez-Vila, X., Dentz, M., 2016. Scale dependence of the hydraulic properties of a fractured aquifer estimated using transfer functions. Water Resour. Res. 52, 5008–5024. https://doi.org/10.1002/2016WR018660.
Pedretti, D., Fernàndez-Garcia, D., Sanchez-Vila, X., Bolster, D., Benson, D.A., 2014. Apparent directional mass-transfer capacity coefficients in three-dimensional anisotropic heterogeneous aquifers under radial convergent transport. Water Resour. Res. 50, 1205–1224. https://doi.org/10.1002/2013WR014578.
Rman, N., Tóth, Gy., 2011. T-JAM Vízföldtani koncepcionális modell (in Hungarian), pp. 25.
Rodríguez-Rodríguez, M., Benavente, J., 2008. Definition of wetland typology for hydro-morphological elements within the WFD. A case study from southern Spain. Water Resour. Manage. 22, 797–821. https://doi.org/10.1007/s11269-007-9193-9.
Ruszkiczay-Rüdiger, Z., Fodor, L.I., Horváth, E., 2007. Neotectonics and quaternary landscape evolution of the Gödöllő Hills, Central Pannonian Basin. Hungary. Global . Planet. Change 58 (1), 181–196. https://doi.org/10.1016/j.gloplacha.2007.02.010.
Sanchez-Vila, X., Guadagnini, A., Carrera, J., 2006. Representative hydraulic conductivities in saturated groundwater flow. Rev. Geophys., 44, paper: RG3002, 10.1029/2005RG000169.
Scanlon, B.R., Mace, R.E., Barrett, M.E., Smith, B., 2003. Can we simulate regional groundwater flow in a karst system using equivalent porous media models? Case study, Barton Springs Edwards aquifer, USA. J. Hydrology 276, 137–158. https://doi.org/10.1016/S0022-1694(03)00064-7.
Schuler, M.S., Cañedo-Argüelles, M., Hintz, W.D., Dyack, B., Birk, S., Relyea, R.A., 2018. Regulations are needed to protect freshwater ecosystems from salinization. Philosophical Transactions of the Royal Society B, Biological Sciences, 374, paper: 20180019, 10.1098/rstb.2018.0019.
Schulze-Makuch, D., 2005. Longitudinal dispersivity data and implications for scaling behavior. Groundwater 43 (3), 443–456. https://doi.org/10.1111/j.1745-6584.2005.0051.x.
Simmons, C.T., Narayan, K.A., 1997. Mixed convection processes below a saline disposal basin. J. Hydrology 194, 263–285. https://doi.org/10.1016/S0022-1694(96)03204-0.
Singh, A., 2020. Salinization and drainage problems of agricultural land. Irrig. Drain. 69 (4), 844–853. https://doi.org/10.1002/ird.2477.
Smith, M.E., Wynn, J.G., Scharping, R.J., Moore, E.W., Garey, J.R., Onac, B.P., 2021. Source of saline groundwater on tidally influenced blue holes on San Salvador Island, Bahamas. Hydrogeol. J. 29, 429–441. https://doi.org/10.1007/s10040-020-02266-z.
Sun, Y., Wendi, D., Kim, D.E., Liong, S.-Y., 2019. Deriving intensity–duration–frequency (IDF) curves using downscaled in situ rainfall assimilated with remote sensing data. Geosci. Lett. 6, 17. https://doi.org/10.1186/s40562-019-0147-x.
Szijártó, M., Galsa, A., Tóth, Á., Mádl-Szőnyi, J., 2019. Numerical investigation of the combined effect of forced and free thermal convection in synthetic groundwater basins. J. Hydrol. 572, 364–379. https://doi.org/10.1016/j.jhydrol.2019.03.003.
Szijártó, M., Galsa, A., Tóth, Á., Mádl-Szőnyi, J., 2021. Numerical analysis of the potential for mixed thermal convection in the Buda Thermal Karst, Hungary. J. Hydrology: Regional Studies, 34, paper: 100783, 10.1016/j.ejrh.2021.100783.
Szocs, T., Rman, N., Süveges, M., Palcsu, L., Tóth, G.y., Lapanje, A., 2013. The application of isotope and chemical analyses in managing transboundary groundwater resources. Appl. Geochem. 32, 95–107. https://doi.org/10.1016/j.apgeochem.2012.10.006.

Tejeda, I., Cienfuegos, R., Muñoz, J.F., Durán, M., 2003. Numerical modeling of saline intrusion in Salar de Atacama. J. Hydrol. Eng. 8 (1), 25–34. https://doi.org/10.1061/(ASCE)1084-0699(2003)8:1(25).

Tóth, J., 2009. Gravitational Systems of Groundwater Flow: Theory, Evaluation, Utilization. Cambridge University Press, United Kingdom, p. 297.

Van Dam, R.L., Simmons, C.T., Hyndman, D.W., Wood, W.W., 2009. Natural free convection in porous media: First field documentation in groundwater. Geophys. Res. Lett., 36, paper: LL11403, 10.1029/2008GL036906.

Vanderborght, J., Vereecken, H., 2007. Review of dispersivities for transport modeling in soils. Vadose Zone J. 6 (1), 29–52. https://doi.org/10.2136/vzj2006.0096.

Varsányi, I., Ó.Kovács, L., 2009. Origin, chemical and isotopic evolution of formation water in geopressured zones in the Pannonian Basin, Hungary. Chem. Geol. 264 (1–4), 187–196. https://doi.org/10.1016/j.chemgeo.2009.03.006.

Vásquez, C., Ortiz, C., Suárez, F., Muñoz, J.F., 2013. Modeling flow and reactive transport to explain mineral zoning in the Atacama salt flat aquifer, Chile. J. Hydrol. 490, 114–125. https://doi.org/10.1016/j.jhydrol.2013.03.028.

Wang, J.-Z., Jiang, X.-W., Wan, L., Wörman, A., Wang, H., Wang, X.-S., Li, H., 2015. An analytical study on artesian flow conditions in unconfined-aquifer drainage basins. Water Resour. Res. 51 (10), 8658–8667. https://doi.org/10.1002/2015WR017104.

Weatherill, D., Simmons, C.T., Voss, C.I., Robinson, N.I., 2004. Testing density-dependent groundwater models: two-dimensional steady state unstable convection in infinite, finite and inclined porous layers. Adv. Water Resour. 27, 547–562. https://doi.org/10.1016/j.advwatres.2004.01.003.

Wen, B., Chang, K. W., Hesse, M.A., 2018. Rayleigh-Darcy convection with hydrodynamic dispersion. Phys. Rev. Fluids, 3, paper: 123801, 10.1103/PhysRevFluids.3.123801.

Werner, A.D., Bakker, M., Post, V.E.A., Vandenbohede, A., Lu, C., Ataie-Ashtiani, B., Simmons, C.T., Barry, D.A., 2013. Seawater intrusion processes, investigation and management: Recent advances and future challenges. Adv. Water Resour. 51, 3–26. https://doi.org/10.1016/j.advwatres.2012.03.004.

Wu, H., Fang, W.-Z., Kang, Q., Tao, W.-Q., Qiao, R., 2019. Predicting effective diffusivity of porous media from images by deep learning. Sci. Rep. 9, 20387. https://doi.org/10.1038/s41598-019-56309-x.

Zhang, J., Zhou, J., Fu, L., Li, H., Lou, D., 2020a. Karstification of Ordovician carbonate reservoirs in Huanghua depression and its control factors. Carbonates Evaporites 35, paper: 42. https://doi.org/10.1007/s13146-020-00572-x.

Zhang, X., Jiao, J.J., Li, H., Luo, X., Kuang, X., 2020b. Effects of downward intrusion of saline water on nested groundwater flow systems. Water Resour. Res., 56, paper: e2020WR028377, 10.1029/2020WR028377.

Zhang, Z.-Y., Jiang, X.-W., Wang, X.-S., Wan, L., Wang, J.-Z., 2018. A numerical study on the occurrence of flowing wells in the discharge area of basins due to the upward hydraulic gradient induced wellbore flow. Hydrol. Process. 32 (11), 1682–1694. https://doi.org/10.1002/hyp.11623.

Zimmermann, W.B.J., 2006. Multiphysics Modeling With Finite Element Methods. World Scientific Publishing Company, Singapore, p. 422.